

FIRST-PRINCIPLES STUDY ON THE $\text{AlAs}_x\text{Sb}_{1-x}$ ALLOYS

NATALIE TAN WEE SIAN

**A project report submitted in partial fulfilment of the
requirements for the award of Bachelor of Science
(Honours) Physics**

**Lee Kong Chian Faculty of Engineering and Science
Universiti Tunku Abdul Rahman**

April 2022

DECLARATION

I hereby declare that this project report is based on my original work except for citations and quotations which have been duly acknowledged. I also declare that it has not been previously and concurrently submitted for any other degree or award at UTAR or other institutions.

Signature : 

Name : Natalie Tan Wee Sian

ID No. : 1803389

Date : 16th May, 2022

APPROVAL FOR SUBMISSION

I certify that this project report entitled “**FIRST-PRINCIPLES STUDY ON THE ALAS_xSB_{1-x} ALLOYS**” was prepared by **NATALIE TAN WEE SIAN** has met the required standard for submission in partial fulfilment of the requirements for the award of Bachelor of Science (Honours) Physics at Universiti Tunku Abdul Rahman.

Approved by,

Signature : _____

Supervisor : Dr. Yeoh Keat Hoe

Date : 16th May, 2022

The copyright of this report belongs to the author under the terms of the copyright Act 1987 as qualified by Intellectual Property Policy of Universiti Tunku Abdul Rahman. Due acknowledgement shall always be made of the use of any material contained in, or derived from, this report.

© 2022, Natalie Tan Wee Sian. All right reserved.

ACKNOWLEDGEMENTS

I would like to express my sincere gratitude to my FYP research supervisor, Ir. Dr. Yeoh Keat Hoe for the opportunity that he has granted me to work on this project. The experience has greatly piqued my interest in the field of condensed matter physics. Dr Yeoh's generous guidance, insight and enormous patience has allowed me to gain a better understanding in my research work and to navigate through a myriad of issues I have encounter during the course of this project.

Furthermore, the completion of this project could not have been possible without the guidance of Associate Prof. Dr. Chew Khian Hooi from the Department of Physics, University Malaya. This project is part of the joint collaboration research with Dr. Chew.

Last but not least, I would like to thank my patient and supportive husband and best friend, Saravanan who has seen me through the best and the worst of times throughout my journey pursuing an undergraduate degree in physics and career change.

I am also truly grateful that I am able to conduct my study and research from home and complete the academic requirements of this project despite the ongoing Covid-19 pandemic and lockdown restrictions imposed nationwide.

ABSTRACT

The work conducted in this project aims to study the composition dependence of the energy gap values, E_g of the ternary alloy composites. The ground-state electronic properties of the $\text{AlAs}_x\text{Sb}_{1-x}$ semiconductor alloy composites were investigated using first-principles calculations of Density Functional Theory (DFT) within the Generalized Gradient Approximation (GGA) functional framework with the implementation of Perdew–Burke–Ernzerhof (PBE) exchange-correlation (XC). Projector Augmented Wave (PAW) pseudopotential was used in performing scalar relativistic calculations with the inclusion of non-linear core corrections of Engel–Vosko (EV93) exchange functional in the optimization of energy potentials and total energy. The energy band gap values of AlAs, AlSb and $\text{AlAs}_x\text{Sb}_{1-x}$ alloys were calculated and discussed, with obtained results mostly in agreement with values reported in theoretical and experimental figures. Band gap energy values obtained in this project for AlAs and AlSb were 1.48 eV and 1.22 eV, respectively. Standard deviation for the x values in $\text{AlAs}_x\text{Sb}_{1-x}$ of 0.25, 0.56 and 0.75 were 0.127 ± 0.003 eV, 0.404 ± 0.003 eV and 0.10 ± 0.001 eV, respectively, while the linear regression slopes for calculated band gap curve and the scissor corrected curve were 0.63 and 0.464, respectively. Deviation of the band gap curve relative to Vegard's linear curve was 0.125 ± 0.005 eV. In conclusion, these results are in accordance with experimental data as well as values reported in literature. It has been shown that there is a non-linear behaviour in the composition dependence, x of the band gap values for the ternary alloys, indicating the digression from Vegard's law, with evident downward bowing of the fundamental energy gap values obtained relative to the alloy fraction composition. There is clear indication of the indirect band gaps via the CBM along the L- and X-paths of the band structures as well as the distinct energy gap dependence on the arsenic composition, x . Recommendations on further study include additional crystal visualizations of supercell structures matching that of $\text{AlAs}_{0.56}\text{Sb}_{0.44}$ that also possess similar BZ structures similar to that of the constituent binaries, identification of the critical x value where crossover from indirect to direct band gap occurs and further attempts to perform calculations that procure results for $\text{AlAs}_x\text{Sb}_{1-x}$ random alloy structures.

TABLE OF CONTENTS

DECLARATION		i
APPROVAL FOR SUBMISSION		ii
ACKNOWLEDGEMENTS		iv
ABSTRACT		v
TABLE OF CONTENTS		vi
LIST OF TABLES		viii
LIST OF FIGURES		ix
LIST OF SYMBOLS / ABBREVIATIONS		xii
LIST OF APPENDICES		xv
CHAPTER		
INTRODUCTION		1
1.1	Introduction to III-V Semiconductor Alloys	1
1.2	Introduction to AlAs, AlSb and AlAs _x Sb _{1-x} Alloy Composites	1
1.3	Problem Statement	2
1.4	Aim and Objectives	4
1.5	Scope and Limitation of the Study	5
1.6	Importance and Contribution of the Study	6
1.7	Outline of the Report	7
2	LITERATURE REVIEW	9
2.1	Density Functional Theory	15
2.2	The Interpolation Scheme	17
2.3	Vegard's Law	19
2.4	Bowing Parameter, <i>b</i>	20
2.5	Structural and Electronic Properties: AlAs, AlSb and AlAs _x Sb _{1-x}	9
2.5.1	Aluminium Arsenide, AlAs	9
2.5.2	Aluminium Antimonide, AlSb	11

2.5.3 Aluminium Arsenide Antimonide, $\text{AlAs}_x\text{Sb}_{1-x}$

12

3	METHODOLOGY AND WORK PLAN	23
3.1	Materials Modelling with Quantum ESPRESSO	23
3.2	Crystal Structure Visualization with VESTA and XCRYSDEN	25
3.3	Performing Electronic-Structure Calculations	33
3.4	XC Functional and Parameters	35
3.5	Work Plan	35
3.6	Work Stages	37
4	RESULTS AND DISCUSSION	39
4.1	Electronic Properties of AlAs and AlSb	40
4.2	Electronic Properties of $\text{AlAs}_x\text{Sb}_{1-x}$	41
5	CONCLUSIONS AND RECOMMENDATIONS	48
5.1	Conclusions	48
5.2	Recommendations for Future Work	48
	REFERENCES	51
	APPENDICES	54

LIST OF TABLES

Table 2.1:	Experimental values of AlAs energy band gap from multiple sources, compared between different XC functionals.	11
Table 2.2:	Experimental values of AlSb energy band gap from multiple sources, compared between different XC functionals.	12
Table 3.1:	Number of Al, As and Sb atoms based on arsenic composition, x according to unit cell matrices.	26
Table 4.1:	Calculated band gap values of binary alloys AlAs and AlSb.	41
Table B-1:	Structural, electronic and optical properties of binary alloys AlAs and AlSb (Adachi, 2017).	56

LIST OF FIGURES

Figure 1.1:	(a) Ball and stick diagram of a zinc blende unit cell. Atomic crystal structure representation of (b) AlAs and (c) AlSb (A. Jain <i>et al.</i> , 2013).	2
Figure 2.1:	PDOS and total DOS calculations on AlAs. The black line indicates Fermi energy level, E_F (Bounab <i>et al.</i> , 2017).	10
Figure 2.2:	Electronic partial and total density of states (PDOS) as a function of the energy for AlSb. The black line indicates Fermi energy level, E_F (Bounab <i>et al.</i> , 2017).	12
Figure 2.3:	(a) Electronic density of states (DOS) as a function of the energy for AlAs _{0.5} Sb _{0.5} . (b) Energy band gap as a function of As composition for AlAs _x Sb _{1-x} computed along the Γ -, X- and L-paths in the BZ. DFT calculations employed are of the LDA scheme (Bounab <i>et al.</i> , 2017).	13
Figure 2.4:	Energy band gap as a function of As composition for AlAs _x Sb _{1-x} . DFT calculations employed are of the WC-GGA scheme. The marked curves are calculated values using EV while the corresponding unmarked lines are scissor-corrected values (El Haj Hassan <i>et al.</i> , 2010).	14
Figure 3.1:	Logo of Quantum ESPRESSO (QEF, 2021).	24
Figure 3.2:	Sample of the terminal window of Ubuntu with executed commands to run computations on QE, from structural relaxation to band structure diagram.	24
Figure 3.3:	Logo and banner of VESTA (Momma, 2021).	25
Figure 3.4:	3D perspective visual representation of AlAs _x Sb _{1-x} digital alloy with interlocking Al layers when unit cell is viewed (a) along the x-axis and (b) from an alternative view. The blue, green and red spheres represent Al, As and Sb, respectively.	25
Figure 3.5:	3D visualization in different orientation of (a) AlSb and (b) AlAs with applied depth perspective and polyhedral shading. The blue, green and red spheres represent Al, As and Sb, respectively.	27
Figure 3.6:	3D projection of AlSb along the (a) x-axis, (b) y-axis and (c) z-axis and (d) angles $\alpha^{(c)}$, $\beta^{(c)}$ and $\gamma^{(c)}$, as indicated	

- lattice parameters a , b and c . Visualization of ‘reciprocal pairs’ of constructed alloy composites (e) $\text{AlAs}_{0.25}\text{Sb}_{0.75}$ and (f) $\text{AlAs}_{0.75}\text{Sb}_{0.25}$. The blue, green and red spheres represent Al, As and Sb, respectively. 28
- Figure 3.7: 3D visualization of the $\text{AlAs}_x\text{Sb}_{1-x}$ digital alloy composites where the value of x is (a) 0, (b) 0.25, (c) 0.38, (d) 0.62, (e) 0.75, (f) 1, and (g) 0.56. The blue, green and red spheres represent Al, As and Sb, respectively. 31
- Figure 3.8: Logo of latest software built version of XCrySDen (Alexp, 2012). 32
- Figure 3.9: 3D visualization of one of the optimised $\text{AlAs}_x\text{Sb}_{1-x}$ alloy composites. 32
- Figure 3.10: Flowchart for DFT calculations using Quantum ESPRESSO. 34
- Figure 3.11: Cropped PAW pseudo-potential script for (a) Al, (b) As and (c) Sb. 36
- Figure 4.1: 3D illustration of finite crystal structure of one possible interdigitated configuration of $\text{AlAs}_x\text{Sb}_{1-x}$. The blue, green and red spheres represent Al, As and Sb, respectively. 39
- Figure 4.2: (a) Band structure diagram of (a) AlAs and (b) AlSb. The red bold arrow indicates the indirect band gap measured between VBM and CBM. 41
- Figure 4.3: Calculated average density of state for $\text{AlAs}_x\text{Sb}_{1-x}$ alloy composite for values of x at (a) 0, (b) 0.25, (c) 0.38, (d) 0.56, (e) 0.62, (f) 0.75 and (g) 1. The red dash line indicates normalised Fermi energy level. $E-E_F$. 44
- Figure 4.4: (a) Composition dependence of calculated energy band gap values with standard deviation bars and (b) shaded error bands with green dotted line representing Vegard’s law. The orange dash line represents Vegard’s law while the red dotted line is the bowed polynomial curve fitting. (c) Comparative analysis of scissor-corrected energy band gap values with experimental figures. The corresponding dotted lines represent Vegard’s law applied to calculated band gap curves. 45
- Figure A-1: Brillouin zones for supercells of x values and cell matrices (a) 0 and 1 ($1 \times 1 \times 1$), (b) 0.25, 0.38, 0.62 and

	0.75 ($2 \times 2 \times 2$), (c) 0.25 and 0.75 ($1 \times 2 \times 2$) and (d) 0.56 ($2 \times 2 \times 4$).	55
Figure C-1:	Sample VESTA output scripts of atomic positions and dimensions in the format of (a) <i>.vasp</i> and (b) <i>.xyz</i> .	58
Figure C-2:	Sample QE input script for structural relaxation VCRELAX parameters.	58
Figure C-3:	Sample QE input script of SCF parameters.	59
Figure C-4:	Sample QE input script of NSCF parameters.	60
Figure C-5:	Sample QE input script of DOS parameters.	61
Figure C-6:	Sample QE input script of BANDS parameters for binary alloy.	61

LIST OF SYMBOLS / ABBREVIATIONS

α	Electron ionization coefficient
α_{th}	Linear thermal expansion coefficient, K ⁻¹
$\alpha^{(c)}$	Angle between b and c lattice parameters, °
β	Hole ionization coefficient
$\beta^{(c)}$	Angle between a and c lattice parameters, °
$\gamma^{(c)}$	Angle between a and b lattice parameters, °
$\delta n(\mathbf{r})$	Electronic density
ϵ_s	Static dielectric constant
ϵ_∞	High-frequency dielectric constant
θ_D	Debye temperature, K
a	Lattice constant, Å
a_{AB}	Equilibrium lattice parameter of binary alloy AB, Å
a_{AC}	Equilibrium lattice parameter of binary alloy AC, Å
a_c	Conduction band deformation potentials, eV
a_{eq}	Alloy equilibrium lattice parameter, Å
a_v, b, d	Valence band deformation potentials, eV
b	Bowing parameter
b_{CE}	Bowing due to charge-exchange
b_{SR}	Bowing due to structural relaxation
b_{VD}	Bowing due to volume deformation
C	Specific heat, J g ⁻¹ K ⁻¹
C_{ij}	Elastic stiffness, dyn cm ⁻²
d_M	Molecular density, Å ⁻³
E_F	Fermi energy level, eV
E_g	Band gap energy, eV
$E_g(x)$	Band gap energy, given Arsenic composition, eV
E_g^Γ	Band gap energy along the BZ Γ -path, eV
E_g^{AlAs}	Energy gap of AlAs, eV
E_g^{AlSb}	Energy gap of AlSb, eV
E_g^L	Band gap energy along the BZ L-path, eV
E^{Total}	Total energy, eV
E_g^X	Band gap energy along the BZ X-path, eV

E_v	Valence band maximum energy, eV
eV	Electron volts
E_{XC}	Exchange correlation functional
k	Wave vector
M	Molecular weight
m_{HH}^*	Density of state heavy hole
m_{LH}^*	Averaged light hole
m_{SO}	Spin orbit split-off effective hole masses
m_e^Γ	Electron effective mass at Γ -conduction band
m_e^X, m_e^L	Density of state mass
m_c^X, m_c^L	Conductivity mass
N_A	Avogadro constant, $6.022 \times 10^{23} \text{ mol}^{-1}$
n_{in}	Input charge density
n_{out}	Output charge density
S_{ij}	Compliance constants, $\text{cm}^2 \text{ dyn}^{-1}$
T	Ternary parameter, temperature, K
T^S	Kinetic energy functional
$V_{ext}(r)$	external potential
V_{XC}	Exchange correlation potential
W	Thermal resistivity, cm K/W
3D	Three-dimensional
Al	Aluminium
APD	Avalanche photodiode
As	Arsenic
BANDS	Band structure
BFGS	Broyden–Fletcher–Goldfarb–Shanno
BZ	Brillouin zone
CBM	Conduction band minimum
CE	Charge-exchange
CIF	Crystallographic Information File
DFT	Density functional theory
DFPT	Density functional perturbation theory
EV/EV93	Engel-Vosko

DOS	Density of states
GGA	Generalized Gradient Approximation
GPU	Graphics processor unit
HHB	Heavy hole bands
H_{KS}	Kohn-Sham Hamiltonian
KS	Kohn-Sham
LDA	Local Density Approximations
LHB	Light hole bands
NSCF	Non-self-consistent field
OS	Operating system
PAW	Projector-Augmented Wave
PBE	Perdew-Burke-Ernzerhof
PDOS	Partial density of states
PP	Pseudo-potential
PROJWFC	Projected wavefunctions, QE functionality
PW	Plane-wave
PWSCF	Plane-wave self-consistent field
QE	Quantum ESPRESSO
Sb	Antimony
SCF	Self-consistent field
SQS	Special Quasi-random Structures
SR	Structural relaxation
UM	Universiti Malaya
VASP	Vienna Ab initio Simulation Package
VBM	Valence band maximum
VBR	Breakdown voltage, V
VCA	Virtual crystal approximation
VCRELAX	Variable-cell relaxation
VD	Volume deformation
VESTA	Visualization for Electronic and STructural Analysis
WC	Wu and Cohen
WC-GGA	Generalized Gradient Approximation of Wu and Cohen
XC	Exchange-correlation
XCrySDen	Crystalline Structures and Densities

LIST OF APPENDICES

APPENDIX A: Figures and Graphs	54
APPENDIX B: Tables	56
APPENDIX C: Computer Command Scripts	58

CHAPTER 1

INTRODUCTION

1.1 Introduction to III-V Semiconductor Alloys

The mechanical, electrical and thermal properties of III-V zinc blende semiconductors have been shown to be highly suitable to be incorporated into high-speed electronic, long-range photonic and optical devices, with III-Antimonides used in high thermal optical and electronic components while III-Arsenides in the fabrication of electric devices (Bounab *et al.*, 2017). The combined ternary alloy consisting of III-Antimonide and III-Arsenide alloys produce materials with properties that are intermediary between the binary compounds. $\text{AlAs}_x\text{Sb}_{1-x}$, one of several notable III-V semiconductor alloys is generally regarded as a wide variable band gap barrier that reaches larger spectral range and has GaSb, InAs and InP substrate matched properties.

1.2 Introduction to AlAs, AlSb and $\text{AlAs}_x\text{Sb}_{1-x}$ Alloy Composites

AlAs, a semiconductor alloy of aluminium and arsenic, has a molar mass of 101.9031 g/mol, the appearance of orange crystals, is soluble in water and ethanol and it is a tetrahedral structure of a Zincblende crystal. AlSb, an alloy of aluminium and antimony is also a Zincblende tetrahedral structure, has the appearance of black crystals, with molar mass of 148.742 g/mol and is insoluble in water. The Zincblende structure, as shown in Figure 1.1 is associated with the geometry coordination of a regular tetrahedron, where each atom has four other neighbouring atoms of another element surrounding it in a tetrahedral cubic formation.

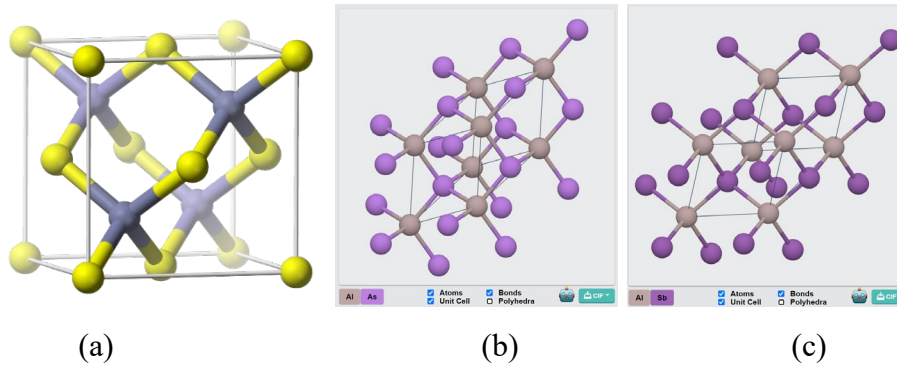


Figure 1.1: (a) Ball and stick diagram of a zinc blende unit cell. Atomic crystal structure representation of (b) AlAs and (c) AlSb (A. Jain *et al.*, 2013).

A semiconductor ternary alloy consists of the combination of three semiconductor elements, the product of which is a new alloy composite semiconductor material that exhibits its own unique structural, optical and electronic properties. Binary alloys can be constructed with other III-V compounds which yields an intermediate ternary alloy, in which case, the focus of this project, $\text{AlAs}_x\text{Sb}_{1-x}$ can be simulated by combining the Aluminium-Arsenide (AlAs) and Aluminium-Antimonide (AlSb) binaries.

The use of III-V ternary alloys is imperative in many optical and electronic devices as they can be optimized and pre-configured to meet specific application requirements, i.e., the potential tunability of the energy bandgap is dependent on the composition and structural configuration of the alloy (Adachi, 2017). Consequently, it becomes essential to optimize alloy compositions and configurations, in order to attain the highest efficiency and reliability (El Haj Hassan *et al.*, 2010).

1.3 Problem Statement

Fast, high performance data communications and light detection systems necessitate the use of highly responsive avalanche photodiodes (APDs) and while the gain component of these devices typically incorporates InAlAs and InP materials, the impact ionization coefficients of electrons (α) and holes (β) produces significant levels of noise when high electric fields are applied. This, thus reduces the overall bandwidth gain and responsivity of the device. In an experiment by Yi *et al.*, it was found that the InP lattice matched ternary alloy

of $\text{AlAs}_{0.56}\text{Sb}_{0.44}$ yields relatively low levels of excess noise. This would suggest that the potential of using this composite alloy could conceivably realise the fabrication of highly sensitive vertically illuminated APD devices and could potentially bring forth the possibility of newly developed high performing receivers that could effectively be employed in sensors and networking applications.

In retrospect, alloys of semiconductor materials have long been the subject of research and studies due to the ability to tune the size of the forbidden energy gap within its band structure. Along with the capability of influencing other material parameters, these alloys can be optimized to be applied in a wide range of semiconductor devices. The results obtained from varying the alloy compositions, geometry, doping concentrations, lattice strain and feature size maximise the viability of integrating small structure systems of superlattices and quantum well into device applications (El Haj Hassan et al., 2010).

Despite the wide array of knowledge and large body of studies on the characteristics and practicality in use of Aluminium-Arsenides and Aluminium-Antimonides, some optical and electronic devices require specific electronic properties that are absent in the abovementioned binary alloys. Furthermore, there is very limited experimental work conducted on $\text{AlAs}_x\text{Sb}_{1-x}$ ternary alloys due to complications concerning computational resources and challenging calculations relating to configurations, arrangements and general disorder within the alloy structures.

The combination of AlAs and AlSb constituent alloys to form $\text{AlAs}_x\text{Sb}_{1-x}$ alloy composites produce intermediate properties that are unique to the ternary alloy. In doing so, the focus of the study in this project is to study and analyse the composition dependence of the energy band gap values. In addition, it was found that varying the composition of its constituent components within the crystal structure of the alloy give rise to a tuneable band gap value that could allow for materials fabrication tuned to required electronic specifications. The study and analysis of ternary alloy $\text{AlAs}_x\text{Sb}_{1-x}$ not only contribute to the lack of theoretical studies on the alloy material but also could facilitate further research and future work into materials modelling of other quaternary alloys, such as $\text{Al}_x\text{Ga}_{1-x}\text{As}_y\text{Sb}_{1-y}$, presenting opportunities in

fabricating and incorporating new materials in future technology and commercial electronic devices.

1.4 Aim and Objectives

This final year research project aims to study the electronic properties of the alloy $\text{AlAs}_x\text{Sb}_{1-x}$ by the method of first-principles study using the construct of the DFT framework. Therein, four objectives are to be met.

The first objective is to carry out literary reviews on AlAs and AlSb binary alloys and $\text{AlAs}_x\text{Sb}_{1-x}$ ternary alloy which is crucial in the aid of further study and deeper understanding of the properties and theoretical concepts associated with the alloy composites. It is through literature review that provides the necessary benchmark and guidelines in our calculations, that we may use as reference and comparison when computational data and results are obtained to verify that selected parameters used in our study are suitable and justified.

The second objective is to study and analyse the electronic properties of ternary alloy $\text{AlAs}_x\text{Sb}_{1-x}$ and its constituent binary alloys, AlAs and AlSb. Properties such as Fermi level, DOS and energy band gap and band structure are to be modelled using DFT, by performing calculations and plotting the density of states and energy band diagrams.

The third objective is to analyse the composition dependence of the energy gaps, E_g of the $\text{AlAs}_x\text{Sb}_{1-x}$ alloys. A series of non-identical interdigitated ternary alloy configurations given selected arsenic composition, x is to be visualized and modelled to obtain the DOS and band gap values. These are then analysed to see how varying compositions and molar fractions of the alloy composites effect energy gaps.

The fourth and final objective is to determine if it obeys Vegard's law. This is based on the rule of mixtures, where it is theorised that a linear relationship exists with regards to the intermediate properties of a material that is made up of two constituent components, each with differing properties, at a given same temperature. Any deviations from Vegard's law are to be measured and analysed.

1.5 Scope and Limitation of the Study

The scope of this project is to study the electronic properties of ternary alloy $\text{AlAs}_x\text{Sb}_{1-x}$, to analyse the composition dependence of energy gap of the alloys and to determine if it obeys Vegard's law. This was implemented through 3D visualizations of the alloy composites using VESTA and XCrySDen as well as DFT calculations within the GGA functional framework using Quantum ESPRESSO (QE).

The structural arrangement of the $\text{AlAs}_x\text{Sb}_{1-x}$ material to be studied is the interdigitated alloy of different arsenic compositions, x , with modelling restricted to a maximum supercell size of 32 atoms due to limited computing resources and time constraint to complete calculations. The duration of the project is 8 months, from June 2021 to September 2021 and from January 2022 to April 2022. Computations were completed from home on a personal computer as well as with remote access to an allocated computing workstation at the Data-intensive Computing Centre (DICC), UM.

One major limitation is the time constraint and the total duration allocated to complete the research project. Often, calculations performed require several weeks to fine-tune and adjust for better accuracy and a complete start-over is sometimes necessary in the case when an error is made in the selected parameters. Often, it also requires time for any additional amendments and recalibration of parameters when analysing the obtained results after protracted computation times. Given the constraint, smaller k point values, as well as larger energy threshold values will have to be chosen to reasonably complete all of the simulations within the time frame, as a compromise to more accurate calculations.

Another prevalent concern is the limited computational processing power necessary to perform more precise calculations of the electronic properties of the alloy structure. As a consequence, a small sample group of alloy configurations achieved by limiting only to smaller supercell matrices is studied for practical computations. In addition, DFT calculations using GGA PBE framework is widely known to underestimate band gap values. As a result, the data obtained may not be truly reflective of the selected configurations and require appropriate adjustments and corrections based on experimental values.

Electronic band structures were not mapped out for some ternary alloy configurations due to significant distortions in the BZ. Therefore, the accuracy of the energy gap values derived from density of state is uncertain. In addition, it is also unclear as to whether the geometry of the alloy crystal structure, cell matrices, size of the alloy supercells, general orientation of the configurations and apparent BZ distortion has any discernible effects on the gap values obtained in this study.

Random alloys were not included as a more comprehensive analysis with interdigitated alloys due to extreme computing resources required and time required for completion. In order to simulate sufficiently isotropic random alloy configurations, supercell sizes have to be sufficiently large. Attempts were made to run computations on a group of random alloy configurations of $3 \times 3 \times 3$ supercells not only yielded results that contradicted with experimental values but also were not completed on time.

1.6 Importance and Contribution of the Study

Despite the vast application potentials in the utility of III-V semiconductor alloys in devices, there is current little theoretical research on $\text{AlAs}_x\text{Sb}_{1-x}$ ternary alloy. This is mainly due to the complexities and difficulties in computational requirements as well as the enormity in the possible arrangements of alloy configurations, which adds to the challenges of completing both experimental and theoretical studies (El Haj Hassan *et al.*, 2010). However, further research can allow us to gain a better understanding on the tuneable properties of these materials and provide a framework to facilitate fabrication of improved devices and introduce new device applications and materials modelling concepts.

Results obtained from this project serves to add research value to the limited number of studies on the composition dependence of the energy band gap and electronic properties of $\text{AlAs}_x\text{Sb}_{1-x}$ ternary alloy. In addition, limitations and recommendations that arise from the study may further promote more concerted and better-defined research efforts in the structural and electronic properties of $\text{AlAs}_x\text{Sb}_{1-x}$ ternary alloys.

1.7 Outline of the Report

The general overview and outline of this project report consists of three main sections, an introduction and aim of the study, review of relevant literature, methodology used and results obtained from this study and lastly, conclusions and recommendations on future studies.

1. INTRODUCTION

- a. Introduction to III-V Semiconductor Alloys
- b. Introduction to AlAs, AlSb and AlAs_xSb_{1-x} Alloy composites
- c. Problem Statement
- d. Aim and Objectives
- e. Scope and Limitation of the Study
- f. Importance and Contribution of the Study

2. BODY

- a. Literature Review
 - i. Introduction
 - ii. Density Functional Theory
 - iii. The Interpolation Scheme
 - iv. Vegard's Law
 - v. Bowing Parameter, b
 - vi. Structural and Electronic Properties
 - Aluminium Arsenide, AlAs
 - Aluminium Antimonide, AlSb
 - Aluminium Arsenide Antimonide, AlAs_xSb_{1-x}
- b. Methodology
 - i. Introduction
 - ii. Materials Modelling with Quantum ESPRESSO
 - iii. Crystal Structure Visualization
 - VESTA
 - XCrySDen
 - iv. Performing Electronic-Structure Calculations
 - v. XC Functional and Parameters

- vi. Work Plan
- vii. Work Stages
- c. Results and Discussion
 - i. Introduction
 - ii. Electronic properties of AlAs and AlSb
 - iii. Electronic Properties of $\text{AlAs}_x\text{Sb}_{1-x}$

3. CONCLUSION

- a. Conclusions
- b. Recommendations for Future Work

CHAPTER 2

LITERATURE REVIEW

2.1 Introduction

In preparation of tasks required to perform visualization and computations in this project, some preliminary research was conducted to gain a better understanding in the scope and breadth of the theoretical concepts and experimental research conducted on the topic. As Quantum ESPRESSO is employed in the electronic-structure calculations and based on DFT, basic comprehension of the theorems, equations and functionals of DFT is soundly rudimentary. Regarding comparative analysis of calculated results obtained in the project, Vegard's law and the associated bowing parameter are practical means of examining the results obtained. Finally, in order to gain an empirical perspective on the system and its constituent binary alloy composites, the general structural and electronic properties of AlAs, AlSb and $\text{AlAs}_x\text{Sb}_{1-x}$ are reviewed.

2.2 Structural and Electronic Properties: AlAs, AlSb and $\text{AlAs}_x\text{Sb}_{1-x}$

There has been a lot of interest generated in III-V semiconductor compounds due to the some of its more favourable characteristics that could potentially be advantageous in device applications. Among them, III-Antimonides and III-Arsenides are of particular interest in device fabrication. Despite the fact, certain optical devices rely on specific parameters that are not found in these binary alloys. Combining them produces new composite alloys that exhibit rather different structural, optical and electronic characteristics that are intermediary of the two binary components. The combination of AlAs and AlSb yields the ternary $\text{AlAs}_x\text{Sb}_{1-x}$ that possesses a large variable bandgap and other properties that is matched to the substrate of InP (Bounab *et al.*, 2017).

2.2.1 Aluminium Arsenide, AlAs

The experiment by Bounab *et al.* based their calculations on the DFT approach implemented with the LDA scheme, employing the XC potential of Ceperley-Alder form within the framework of Perdew and Zunger. Through virtual crystal

approximation (VCA), the Hartwigsen-Goedecker-Hutter scheme with cut-off energy value set at 80 Ha and k-grid of $8 \times 8 \times 8$ was used in the computations (Bounab *et al.*, 2017). The lattice constant, a obtained was 5.61 Å, with indirect band gap ($\Gamma \rightarrow X$), E_g of 1.33 eV, the latter of which is an underestimation of about 40% due to the combined DFT and LDA functional. The PDOS calculation is shown in Figure 2.1.

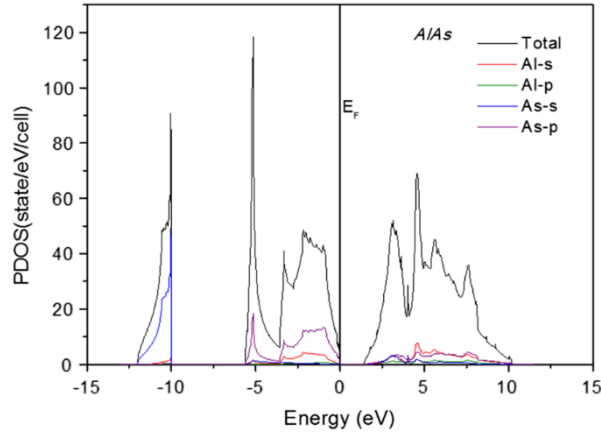


Figure 2.1: PDOS and total DOS calculations on AlAs. The black line indicates Fermi energy level, E_F (Bounab *et al.*, 2017).

The fact that DFT WC-GGA employed in the calculations is widely known to also underestimate energy gap values renders is unsuitable for calculations involving materials in the excited state (El Haj Hassan *et al.*, 2010). GGA, however, produces acceptable electronic band structures in terms of ordering and shape of energy bands that are in close accordance with experimental figures. The EV approach is also inclusively engaged within the functional of the scheme to more accurately compute exchange potentials, yielding improved calculations of lattice constants, energy band gap and band splitting.

It has been shown by El Haj Hassan *et al.* that AlAs produces indirect band gap in the CBM order of X, L and Γ k-paths. Calculations performed using DFT method of FP-LAPW+lo scheme, scalar-relativistic, of WC-GGA, PBE and EV exchange correlation revealed lattice constants of 5.678 Å (WC) and 5.736 Å (PBE). The band gap found through WC was 1.861 eV and with EV was 2.104 eV.

Other experimental values reported include: Lattice constant of 5.661 Å and bandgap of 2.202 eV by Hussain *et al.*, as well as crystal constant of 5.661 Å and indirect bandgap of 2.170 by Adachi. Table 2.1 tabulates other band gap values reported by other authors.

Table 2.1: Experimental values of AlAs energy band gap from multiple sources, compared between different XC functionals.

Sources	XC Functional	Band gap (eV)
Heyd <i>et al.</i>, 2005	PBE	1.62
Hinuma <i>et al.</i>, 2014	PBE	1.32
Tran and Blaha, 2017	PBE	1.45
Wadehra <i>et al.</i>, 2010	PBE (E_g^X)	1.50
Wadehra <i>et al.</i>, 2010	PBE (E_g^Γ)	1.78
Bounab <i>et al.</i>, 2017	LDA	1.33
Tran and Blaha, 2017	LDA	1.35
El Haj Hassan <i>et al.</i>, 2010	WC-GGA	1.86
El Haj Hassan <i>et al.</i>, 2010	EV	2.10
Tran and Blaha, 2017	EV93PW91	1.90

2.2.2 Aluminium Antimonide, AlSb

Computed lattice constant, a for AlSb was 6.09 Å and is in good agreement with experimental values reported by Meyer, 2001 of 6.135 Å (Bounab *et al.*, 2017). Similar to AlAs in section 2.2.1, bandgap energy, E_g was 1.14 eV and this value is underestimated when compared to experimental band gap value of 1.696 eV. The PDOS is showed in the following diagram in Figure 2.2.

Lattice constants, a reported by El Haj Hassan *et al.* were 6.160 Å via WC and 6.232 Å using PBE. It has been shown that, like AlAs, AlSb also has indirect band gap in the CBM order of X, L and Γ k-paths. The bandgap values obtained are 1.343 eV for WC and 1.470 eV for EV. Hussain *et al.* and Adachi both obtained lattice constant 6.136 Å with 1.696 eV bandgap level. Other notable band gap values reported by other works are listed in Table 2.2.

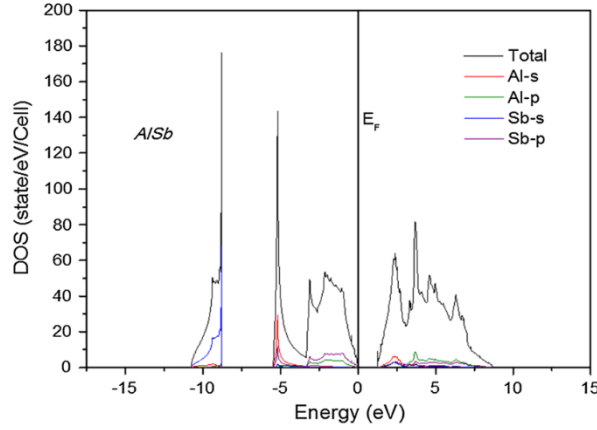


Figure 2.2: Electronic partial and total density of states (PDOS) as a function of the energy for AlSb. The black line indicates Fermi energy level, E_F (Bounab *et al.*, 2017).

Table 2.2: Experimental values of AlSb energy band gap from multiple sources, compared between different XC functionals.

Sources	XC Functional	Band gap (eV)
Heyd <i>et al.</i>, 2005	PBE	1.40
Hinuma <i>et al.</i>, 2014	PBE	0.99
Tran and Blaha, 2017	PBE	1.22
Wadehra <i>et al.</i>, 2010	PBE (E_g^X)	1.29
Wadehra <i>et al.</i>, 2010	PBE (E_g^I)	1.28
Bounab <i>et al.</i>, 2017	LDA	1.14
Tran and Blaha, 2017	LDA	1.15
El Haj Hassan <i>et al.</i>, 2010	WC-GGA	1.34
El Haj Hassan <i>et al.</i>, 2010	EV	1.47
Tran and Blaha, 2017	EV93PW91	1.56

2.2.3 Aluminium Arsenide Antimonide, $\text{AlAs}_x\text{Sb}_{1-x}$

For results reported by Bounab *et al.*, 2017, VCA was utilised for the ternary alloy computations, which demonstrated some upward bowing parameter of around -0.19 \AA for the lattice parameters of $\text{AlAs}_x\text{Sb}_{1-x}$, largely due to the discrepancies between the lattice constants of the two constituent binary alloys. In addition, there is evident variations of non-linear increase of the indirect energy gap values, particularly along the Γ , X and L k-paths relative to the arsenic composition, x in the zinc blende structure of the ternary alloy configurations. Figure 2.3 displays the obtained DOS and LDA energy gap results.

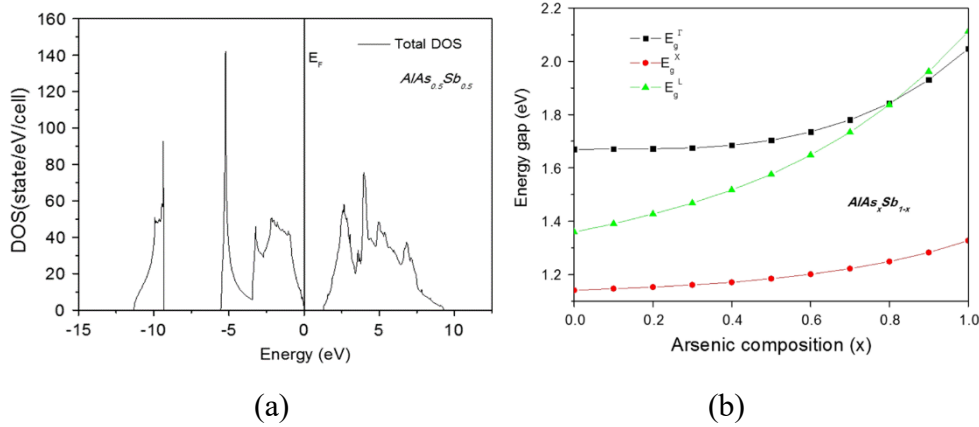


Figure 2.3: (a) Electronic density of states (DOS) as a function of the energy for AlAs_{0.5}Sb_{0.5}. (b) Energy band gap as a function of As composition for AlAs_xSb_{1-x} computed along the Γ -, X- and L-paths in the BZ. DFT calculations employed are of the LDA scheme (Bounab *et al.*, 2017).

It has been shown that the energy bandgap values display quadratic dependence on the composition of the alloy and is highly non-linear (Adachi, 2017). The valence band maximum (VBM) energy, E_v for ternary alloy AlAs_xSb_{1-x} is found along the Γ -point in the Brillouin zone, BZ, where the wave vector is given by the expression (Equation 2.26)

$$k = \frac{2\pi}{a}(0,0,0) \quad (2.1)$$

where

k = wave vector

a = lattice constant

Consequently, it has been found that the conduction band minimum (CBM) energy, E_g^X or E_g^L for AlAs_xSb_{1-x} is detected at either the X-point or L-point in the BZ, respectively with the following expression (Equation 2.27) denoting the wave vector

$$k = \frac{2\pi}{a}(0,0,1) \quad (2.2)$$

where

k = wave vector

a = lattice constant

The minimum indirect bandgap, correspondingly refers to the shift from the VBM at Γ -point to the CBM along the X-point or L-point, relative to the composition of the As and Sb, with the ternary compounds aptly taking on the intermediate nature between the two binary alloy composites.

Due to systematic errors that contribute to the underestimation of energy gap values in both the LDA and GGA DFT computations, the scissor-correction scheme is rigorously employed to perform a defined shift of the forbidden band gap structures (El Haj Hassan *et al.*, 2010). To account for the discrepancies for the ternary alloy composites, experimental energy gap values of the constituent binary compounds are fitted with the calculated energy gap bowing parameters obtained (See Figure 2.4).

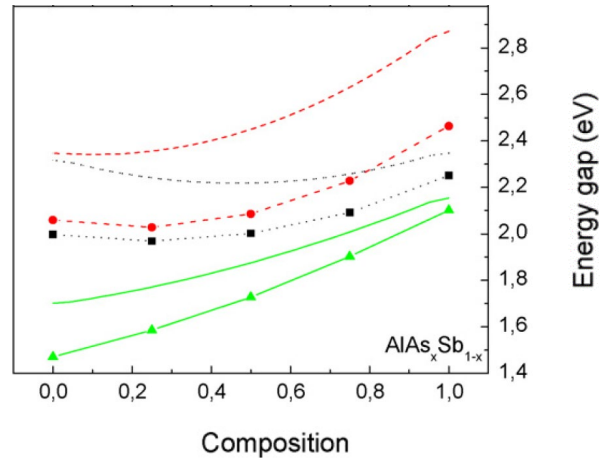


Figure 2.4: Energy band gap as a function of As composition for $\text{AlAs}_x\text{Sb}_{1-x}$. DFT calculations employed are of the WC-GGA scheme. The marked curves are calculated values using EV while the corresponding unmarked lines are scissor-corrected values (El Haj Hassan *et al.*, 2010).

2.3 Density Functional Theory

The proposed theory put forth by Pierre Hohenberg, Walter Kohn and Lu Jeu Sham when applying computational approach to N-electron systems to take into account the density of electrons, $n(\mathbf{r})$ when increasing numbers of particles are introduced to the model of condensed matter. This approach is coined as Density Functional Theory (DFT), which is based on the theorems of Hohenberg-Kohn, is implemented via the Kohn-Sham (KS) approach (Rubio and Marques, 2009). In essence, the theorems state that the density of ground-state electrons, $n(\mathbf{r})$ measures the external potential, $V_{ext}(\mathbf{r})$. Hence, as a result, Equation 2.1 expresses the total energy as a function of $n(\mathbf{r})$

$$E^{Total}[n(\mathbf{r})] = F[n(\mathbf{r})] + \int V_{ext}(\mathbf{r})n(\mathbf{r})d\mathbf{r} \quad (2.3)$$

where the coulomb interaction, T^S as well as the exchange correlation functional, E^{XC} are embedded in the $F[n(\mathbf{r})]$ term, as shown in Equation 2.2

$$F[n(\mathbf{r})] = T^S[n(\mathbf{r})] + \frac{e^2}{2} \iint \frac{n(\mathbf{r})n(\mathbf{r}')}{|\mathbf{r}-\mathbf{r}'|} d\mathbf{r}d\mathbf{r}' + E^{XC}[n(\mathbf{r})] \quad (2.4)$$

Given the constraint of the electronic density $\delta n(\mathbf{r})$ in the following expression (Equation 2.3)

$$\int \delta n(\mathbf{r})d\mathbf{r} = \int \delta\psi_i^*(\mathbf{r})\psi_i(\mathbf{r})d\mathbf{r} = 0 \quad (2.5)$$

when we apply this to the variational calculation, we obtain (Equation 2.4)

$$\delta[E^{Total} - \sum_i \varepsilon_i (\langle \psi_i | \psi_i \rangle - 1)] = 0 \quad (2.6)$$

This, thus, gives us the Kohn-Sham equations (Equation 2.5) for systems without perturbation, where the Kohn-Sham Hamiltonian (H_{KS}) is highlighted in brackets

$$\left[-\frac{\hbar^2}{2m} \nabla_r^2 + V_{SCF}(\mathbf{r}, n(\mathbf{r})) \right] \psi_i(\mathbf{r}) = \varepsilon_i \psi_i(\mathbf{r}) \quad (2.7)$$

where

V_{SCF} = Self-consistent field potential

$\psi_i(\mathbf{r})$ = Kohn-Sham orbitals

By an iterative method, the effective potential, V_{SCF} must self-consistently be solved. The definition of V_{SCF} is given in Equation 2.6

$$V_{SCF}(\mathbf{r}, n(\mathbf{r})) = V_{ext}(\mathbf{r}) + e^2 \int \frac{n(\mathbf{r}')}{|\mathbf{r}-\mathbf{r}'|} d\mathbf{r}' + \frac{\delta E^{XC}[n(\mathbf{r})]}{\delta n(\mathbf{r})} \quad (2.8)$$

$V_{ext}(\mathbf{r})$ is the external potential. The last term in Equation 2.6 is denoted by V_{XC} is the exchange-correlation potential. For self-consistency, the Kohn-Sham equations (Equation 2.5) can be calculated repeatedly within a self-consistent cycle. The loops continuously iterate during implementation until the variation value between input charge density, n_{in} and output charge density, n_{out} is lower than that of a specified threshold value. Every loop of self-consistent calculations yields an updated output charge density value.

The following expression for the ground-state charge density gives is based on the Kohn-Sham approach for the system of non-interacting electrons (Equation 2.7)

$$n(\mathbf{r}) = 2 \sum_{n=1}^{N/2} |\psi_n(\mathbf{r})|^2 \quad (2.9)$$

For every $N/2$ number of low-level orbitals within the non-magnetic system, the Pauli Exclusion Principle is never violated. The kinetic energy functional, thus is given by Equation 2.8

$$T^S[n(\mathbf{r})] = -2 \frac{\hbar}{2m} \sum_{n=1}^{N/2} \int \psi_n^*(\mathbf{r}) \frac{\partial^2 \psi_n(\mathbf{r})}{\partial \mathbf{r}^2} d\mathbf{r} \quad (2.10)$$

Substituting Equation 2.8 into the Schrödinger equation and incorporating the Kohn-Sham eigenvalues ε_n , we obtain (Equation 2.9)

$$-2 \frac{\hbar}{2m} \sum_{n=1}^{N/2} \int \psi_n^*(\mathbf{r}) \frac{\partial^2 \psi_n(\mathbf{r})}{\partial \mathbf{r}^2} d\mathbf{r} = 2 \sum_{n=1}^{N/2} \varepsilon_n \quad (2.11)$$

Using algebraic manipulation, Equation 2.6 is rearranged to find for $V_{ext}(\mathbf{r})$ and, thus we get (Equation 2.10)

$$V_{ext}(r) = V_{SCF}(r, n(r)) - e^2 \int \frac{n(\mathbf{r}')}{|\mathbf{r}-\mathbf{r}'|} d\mathbf{r}' - V^{XC}(\mathbf{r}) \quad (2.12)$$

By substituting Equations 2.2, 2.9 and 2.10 into Equations 2.1, we eventually get the ground-state level of the system (Equation 2.11)

$$E^{Total}[n(\mathbf{r})] = 2 \sum_{n=1}^{N/2} \varepsilon_n - \frac{e^2}{2} \iint \frac{n(\mathbf{r})n(\mathbf{r}')}{|\mathbf{r}-\mathbf{r}'|} d\mathbf{r}d\mathbf{r}' + E^{XC}[n(\mathbf{r})] - \int V^{XC}(\mathbf{r})n(\mathbf{r})d\mathbf{r} \quad (2.13)$$

By expressing the ground-state energy, E^{Total} with respect to charge density $n(\mathbf{r})$, the DFT method used in this project by first-principles serves to measure the atomic positions of the geometrically optimized structures of AIAs and AISb as well as AIAs_xSb_{1-x} alloys and to compute the final energy at ground-state through self-consistent calculations.

2.4 The Interpolation Scheme

Many optoelectronic and electronic transport devices use composite alloys of III-V semiconducting materials and has driven much focus on the study of the electronic band structure of III-V compounds consisting of specific alloy compositions. The energy bandgap, E_g and crystal constant, a for a ternary alloy is independently distinct from its constituents and thus, any resolution to determine the mechanical and electronic parameters are restricted by the scarcity of data and material information available. One approach adopted is defined by the interpolation scheme, which involves some values of known endpoint binary parameters (Adachi, 2017). Hence, ternary alloys may then be constructed initially from its binary alloy components. In some composite alloys, changes to the electronic, optical and structural characteristics are due to the

self-organizing process of spontaneous arrangement within semiconductor alloys, which are known to occur during the epitaxial growth phase.

Implementing the linear interpolation scheme, Equation 2.12 allows the calculation of the ternary parameter, T that is based on the binary parameters for the structure of alloy in the form of $A_xB_{1-x}C$, given that $a \equiv B_{BC}$ and $b \equiv B_{AC} - B_{BC}$

$$T_{A_xB_{1-x}C} = xB_{AC} + (1 - x)B_{BC} \equiv a + bx \quad (2.14)$$

The material characteristics of the ternary material, thus can be accurately extrapolated by the following Equation 2.13, where c , in this particular instance represents what is known as the bowing parameter and that $a \equiv B_{BC}$ and $b \equiv B_{AC} - B_{BC} + C_{A-B}$, and $c \equiv -C_{A-B}$.

$$T_{A_xB_{1-x}C} = xB_{AC} + (1 - x)B_{BC} + C_{A-B}x(1 - x) \equiv a + bx + cx^2 \quad (2.15)$$

The lattice constant, a appears to linearly change according to the alloy composition, which obeys Vegard's law. The lattice parameters and other characteristics of interest of binary alloys AlAs and AlSb, which can be produced using Vegard's law are tabulated in (Table B-1, Appendix), all of which are parameters that are briefly discussed in this section and are calculated values at $T = 300$ K. The expression in Equation 2.14 calculates the molecular density, d_M

$$d_M = \frac{4}{a^3} \quad (2.16)$$

While the expression 2.15 for X-ray crystal density, g can be obtained

$$g = \frac{Md_M}{N_A} \quad (2.17)$$

where

M = Molecular weight

N_A = Avogadro constant, $6.022 \times 10^{23} \text{ mol}^{-1}$

2.5 Vegard's Law

Vegard's law is a heuristic approach to empirical research of materials and crystallography (Ashcroft, 1991). Synonymous to the rule of mixtures, it was found that the lattice properties consisting of two different compounds of a solid solution can be appropriated to be a weighted average of the lattice parameters of those two constituent materials, as shown in the following expression (Equation 2.16)

$$a_{A(1-x)Bx} = (1 - x)a_A + xa_B \quad (2.18)$$

where

a = Lattice constant

A = Atom, element, compound or component 1

B = Atom, element, compound or component 2

x = Composition of B

The empirical finding can also be applied to other structural and electronic properties of materials, such as energy band gap. Given this, as shown in Equation 2.17, the expression thus becomes

$$E_g^{AlAs_xSb_{1-x}} = xE_g^{AlAs} + (1 - x)E_g^{AlSb} \quad (2.19)$$

where

E_g = Energy gap, eV

x = As composition

It is generally assumed that the law is applied to a material where its two components, A and B are pure constituents and possess identical crystal structure. Although Vegard's law is rarely in agreement with experimental values, which can be seen as deviations from the theorized linearity, it can provide useful estimation where experimental values are absent and inconclusive (King, 1966). Vegard's law can also be used to approximate specific compositions or molar fraction for systems that are known to obey the

linear proportionality closely by obtaining known lattice parameters from crystal diffraction methods.

In calculating the band gap energy values in semiconductors, the linear interpolation may be insufficient to accurately describe the gap function. An additional term is thus included as a function of the composition of the alloy composites to address the non-linearity of the energy gap values. This added correction that represents the curvature is attributed by the bowing parameter, b .

2.6 Bowing Parameter, b

In grasping the physical representation of the bowing parameter, b arose from three contributing factors, which includes volume deformation, charge-exchange, as well as structural relaxation (Zunger, 1986). Assuming the ternary alloy composite of AB_xC_{1-x} , with varying shared composition, x , if x is given as 0.5, the general band gap bowing coefficient is thus indicative of the change in the energy gap values, given in the following Equation 2.18

$$AB(a_{AB}) + AC(a_{AC}) \rightarrow AB_{0.5}C_{0.5}(a_{eq}) \quad (2.20)$$

where

a_{AB} = Equilibrium lattice parameter of binary alloy AB

a_{AC} = Equilibrium lattice parameter of binary alloy AC

a_{eq} = Alloy equilibrium lattice parameter

Bowing due to volume deformation (VD), given by b_{VD} , represents the energy gap variation of compressed and dilated bulk materials from the individual corresponding equilibrium lattice parameters to the intermediate alloy composite, given that lattice constants, a is $a(x)$, as shown in the following expression, Equation 2.19

$$AB(a_{AB}) + AC(a_{AC}) \xrightarrow{VD} AB(a) + AC(a) \quad (2.21)$$

Therefore, as shown in Equation 2.20, volume deformation becomes

$$b_{VD} = 2[\varepsilon_{AB}(a_{AB}) - \varepsilon_{AB}(a) + \varepsilon_{AC}(a_{AC}) - \varepsilon_{AC}(a)] \quad (2.22)$$

Bowing due to charge-exchange (CE), given by b_{CE} , denotes the energy band gap variation when the constituent atoms are modelled and simulated together, within the pre-determined lattice constant, a , prior of any relaxation performed on the sublattice, as highlighted in the following expression in Equation 2.21

$$AB(a) + AC(a) \xrightarrow{CE} AB_{0.5}B_{0.5}(a) \quad (2.23)$$

The charge-transfer effects relating to the bonding behaviours of both the binary alloy composite constituents are also included. Hence, the charge transfer attributes affect the bowing in the following manner (Equation 2.22)

$$b_{CE} = 2[\varepsilon_{AB}(a) + \varepsilon_{AC}(a) - 2\varepsilon_{ABC}(a)] \quad (2.24)$$

In relation to overall bowing due to structural relaxation (SR), where structural relaxation is performed on the alloy composites, changes are measured between unrelaxed state and the relaxed alloy, given by b_{SR} in the following Equations 2.23 and 2.24, where subsequently, the total sum of bowing attributes b_{VD} , b_{CE} and b_{SR} , thus produces the total bowing parameter, b .

$$AB_{0.5}C_{0.5}(a) \xrightarrow{SR} AB_{0.5}C_{0.5}(a_{eq}) \quad (2.25)$$

$$b_{SR} = 4[\varepsilon_{ABC}(a) - \varepsilon_{ABC}(a_{eq})] \quad (2.26)$$

Bowing parameter, b , which can be obtained from the parabolic order term of the second order polynomial fitting to the energy gap data, assists in investigating the band gap trend and linearity of the curve. The following expression, Equation 2.25, includes the bowing parameter in the calculation of the bandgap energy of alloy composites with variable As concentration, x

$$E_g(x) = xE_g^{AlAs} + (1-x)E_g^{AlSb} - bx(1-x) \quad (2.27)$$

where

$E_g(x)$ = Analytical energy gap, given value x

E_g^{AlAs} = Energy gap of AlAs

E_g^{AlSb} = Energy gap of AlSb

A positive value of b indicates downward bowing or upward concavity, while a negative bowing parameter represents upward bowing or downward concavity of the curve.

CHAPTER 3

METHODOLOGY AND WORK PLAN

3.1 Introduction

The vast proportion of the computations carried out using QE and XCrySDen for this project were implemented on a workstation physically located in Universiti Malaya, which was remotely accessed with permission extended by Assoc. Prof. Dr. Chew from the time of my industrial training at UM. Coupled with the external computational resources available, visualizations of the binary and ternary alloy composites were performed using a personal computer.

For binary alloys AlAs and AlSb, visualizations were completed through VESTA, from which calculations were then initiated through QE for structural relaxation, density of state and band structure computations, from which the energy band gap was obtained. XCrySDen was employed to visualise and determine k-points within the BZ. The same process was applied for the ternary alloy configurations, with the exception of the k-point visualizations and band structure calculations. Energy gap values were derived from the DOS data. Pseudopotential scripts for Al, As and Sb were retrieved from online PPs libraries sourced from QE and PS Library (Dalcorso, 2012; QEF, 2019).

3.2 Materials Modelling with Quantum ESPRESSO

Quantum ESPRESSO (QE) is used in the DFT calculations of this research project (Refer to Figure 3.1). Developed under GNU General Public License and distributed as a free open-source integrated software package for first-principle calculations of materials modelling and electronic structure, the basis of QE is of DFT, DFPT, pseudopotentials, and plane waves (Giannozzi, et al., 2002). With the latest QE-6.8 version released in July 2021, QE has expanded into an open-source project that promotes independent and collaborated commands. The QE suite is downloadable for use in Linux operating system, with its core components and packages written in the Fortran-90 programming language. Although there are other similar and comparable free open-source packages available that employs the DFT just as QE, such as ABINIT, BigDFT,

and Vienna Ab initio Simulation Package (VASP), QE is selected due to the low processing resources and GPU requirement in performing calculations, as well as the wide availability of parallel and I/O library resources.



Figure 3.1: Logo of Quantum ESPRESSO (QEF, 2021).

QE supports ground-state calculations such as Kohn-Sham orbitals, ultrasoft and norm-conserving pseudopotentials, structural optimization and response characteristics of phonon dispersions, quantum transport as well as spectroscopic properties (Giannozzi *et al.*, 2017). The main features used in this project are the calculations of the total energies of the self-consistent field (SCF), which are performed by executable sub-packages within the suite, i.e., PW, DOS, BANDS, and PROJWFC (See Figure 3.2). Output files of SCF and NSCF calculations produce the bandgap and Fermi energy levels, the sub-package executable BANDS calculates the electronic band structure while DOS and PROJWFC allow for the calculation of the density of states and projected DOS results.

```

user@user-Precision-T5600: ~/Desktop/Natalie/Current_Working/ALAs_bands (2)
File Edit View Search Terminal Help
user@user-Precision-T5600:~/Desktop/Natalie/Current_Working/ALAs_bands (2)$ mpir
un -np 6 /home/user/Downloads/qe-6.5/bin/pw.x <ALAs.vc relax.in > ALAs.vc relax.ou
t
user@user-Precision-T5600:~/Desktop/Natalie/Current_Working/ALAs_bands (2)$ mpir
un -np 6 /home/user/Downloads/qe-6.5/bin/pw.x <ALAs.scf.in > ALAs.scf.out && mpi
run -np 6 /home/user/Downloads/qe-6.5/bin/pw.x <ALAs.nscf.in > ALAs.nscf.out &&
mpirun -np 6 /home/user/Downloads/qe-6.5/bin/dos.x <ALAs.dos.in > ALAs.dos.out
user@user-Precision-T5600:~/Desktop/Natalie/Current_Working/ALAs_bands (2)$ mpir
un -np 6 /home/user/Downloads/qe-6.5/bin/pw.x <ALAs.bands.in > ALAs.bands.out &&
mpirun -np 6 /home/user/Downloads/qe-6.5/bin/bands.x <ALAs.band.in > ALAs.band.
out && mpirun -np 6 /home/user/Downloads/qe-6.5/bin/projwfc.x <ALAs.projwfc.in >
ALAs.projwfc.out
Note: The following floating-point exceptions are signalling: IEEE_DENORMAL
user@user-Precision-T5600:~/Desktop/Natalie/Current_Working/ALAs_bands (2)$ /hon
e/user/Downloads/qe-6.5/bin/plotband.x
Input file > ALAs.band
Reading 8 bands at 101 k-points
Range: -7.1198 14.6148eV Emin, Emax > -12 12
high-symmetry point: 0.5000-0.5774 0.2041 x coordinate 0.0000
high-symmetry point: 0.0000-0.5774 0.2041 x coordinate 0.5000
high-symmetry point: 0.0000 0.0000 0.0000 x coordinate 1.1124
high-symmetry point: 0.5000-0.2887 0.4082 x coordinate 1.0195
high-symmetry point: 0.5000-0.5774 0.2041 x coordinate 2.1730
high-symmetry point: 0.3750-0.6495 0.0000 x coordinate 2.4230
output file (gnuplot/xmgr) > ALAs.band.xmgr
bands in gnuplot/xmgr format written to file ALAs.band.xmgr

output file (ps) > ALAs.band.ps
Efermi > 4.622
deltaE, reference E (for tics) 1.0, 4.622
bands in PostScript format written to file ALAs.band.ps

user@user-Precision-T5600:~/Desktop/Natalie/Current_Working/ALAs_bands (2)$

```

Figure 3.2: Sample of the terminal window of Ubuntu with executed commands to run computations on QE, from structural relaxation to band structure diagram.

3.3 Crystal Structure Visualization with VESTA and XCrySDen

VESTA, which is an acronym for Visualization for Electronic and STructural Analysis allows for 3D visualization of structural, volumetric and crystal morphological data of lattice structures and atomic models (See Figure 3.3). It is a closed-source code and copyrighted visualization software that is freely and publicly distributed for the purpose of educational, scientific, academic and non-commercial research (Koichi Momma, 2011).

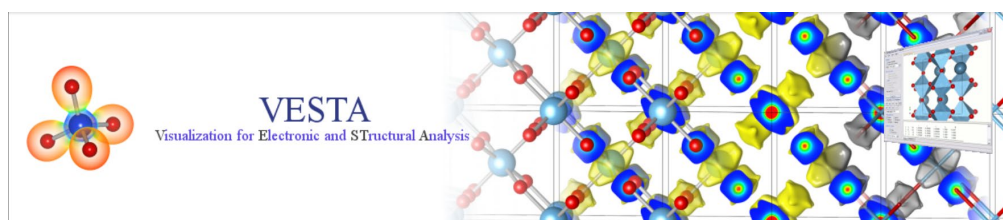


Figure 3.3: Logo and banner of VESTA (Momma, 2021).

VESTA version 3.5.7, built in Jan 2021 was used in the 3D visualization of the AIAs, AISb and AIAs_xSb_{1-x} alloy compositions and the various corresponding configurations in this project. The alloy unit cells visualized were interdigitated configurations, with interlocking Aluminium (Al) between different arrangements of As and Sb atoms to produce digital AIAs_xSb_{1-x} alloy composites, as shown in Figure 3.4.

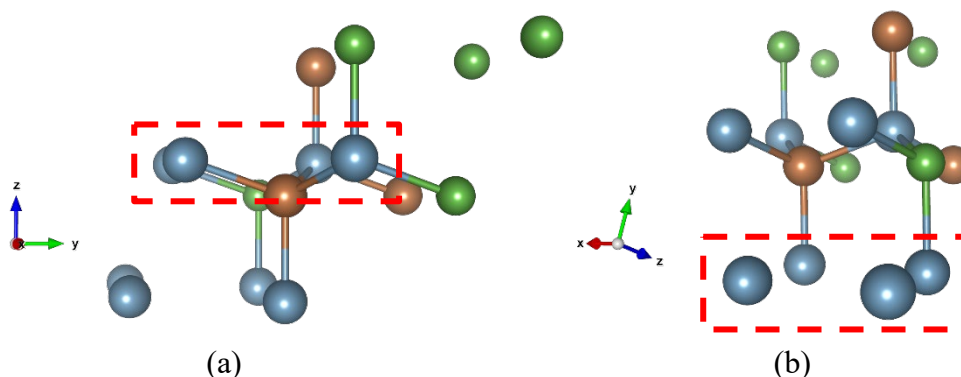


Figure 3.4: 3D perspective visual representation of AIAs_xSb_{1-x} digital alloy with interlocking Al layers when unit cell is viewed (a) along the x-axis and (b) from an alternative view. The blue, green and red spheres represent Al, As and Sb, respectively.

The arsenic (As) composition, x , of the alloys were varied between 0 and 1 and were selected based on procuring the closest empirical formula that gives the smallest possible repeat unit cells, due to limited computational resource and time to complete the project. The atomic units were limited to a maximum of 32 atoms to allow computations to be completed on time, which has allowed for a specific selection of cell matrices that yields the closest round number of atoms to be accurately modelled. The unit cells visualized were of the matrices $1 \times 2 \times 2$ and $2 \times 2 \times 2$ for $\text{AlAs}_{0.25}\text{Sb}_{0.75}$ and $\text{AlAs}_{0.75}\text{Sb}_{0.25}$, $2 \times 2 \times 2$ for $\text{AlAs}_{0.38}\text{Sb}_{0.62}$ and $\text{AlAs}_{0.62}\text{Sb}_{0.38}$ and $2 \times 2 \times 4$ for $\text{AlAs}_{0.56}\text{Sb}_{0.44}$ (Refer to Table 3.1).

Table 3.1: Number of Al, As and Sb atoms based on arsenic composition, x according to unit cell matrices.

Number of atoms									
Matrices	$1 \times 2 \times 2$			$2 \times 2 \times 2$			$2 \times 2 \times 4$		
Arsenic composition (x)	Al	As	Sb	Al	As	Sb	Al	As	Sb
0.25	4	1	3	8	2	6			
0.38				8	3	5			
0.56							16	9	7
0.62				8	5	3			
0.75	4	3	1	8	6	2			

The supercells of the $\text{AlAs}_x\text{Sb}_{1-x}$ alloy compositions were constructed in all possible interdigitated non-identical configurations. This gives a total of 55 different alloy composites, with x values of 0, 0.25, 0.38, 0.56, 0.62, 0.75 and 1, each having 1, 3, 4, 39, 4, 3 and 1 arrangements, respectively. The conventional cell dimensions and atomic positions of binary alloys AlSb and AlAs, where x value is 0 and 1, respectively, were obtained from *.cif* script files, as shown in Figure 3.5 (Jain *et al.*, 2013). The ternary alloy configurations were visualized in periodic construct from the conventional crystal structure of AlSb, where relevant atoms were fastidiously placed in order to achieve a varied set of arrangements.

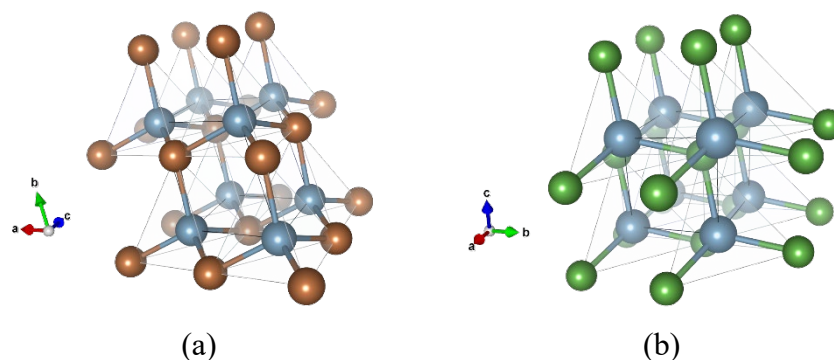
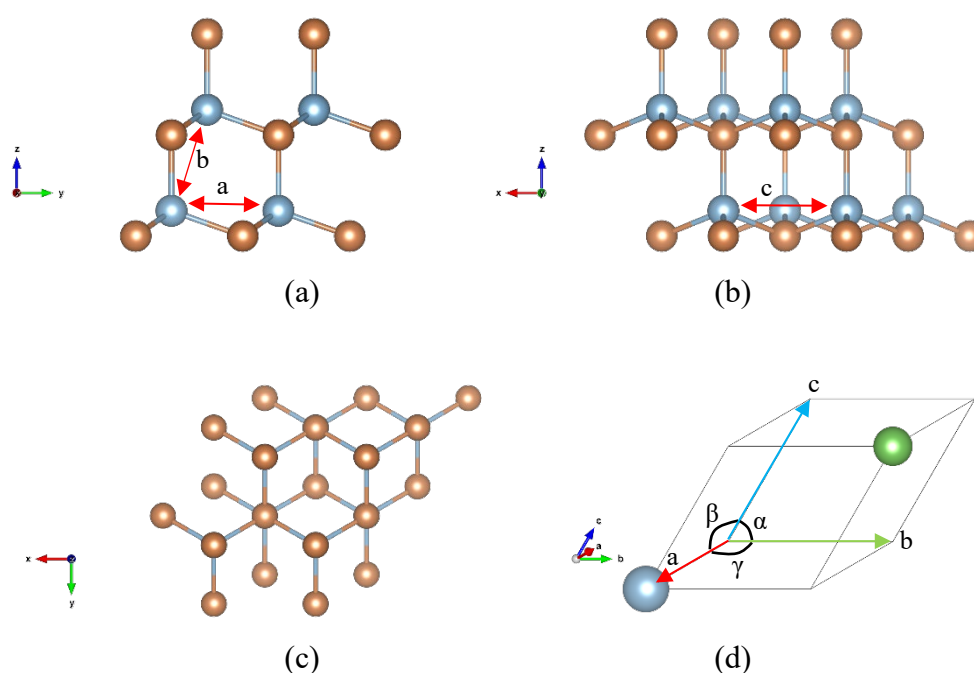


Figure 3.5: 3D visualization in different orientation of (a) AlSb and (b) AlAs with applied depth perspective and polyhedral shading. The blue, green and red spheres represent Al, As and Sb, respectively.

The primary crystal structure from which all subsequent configurations were derived from is of the triclinic lattice, with non-perpendicular axes $\alpha^{(\circ)}$, $\beta^{(\circ)}$ and $\gamma^{(\circ)}$ at 60° and normalised lattice parameters a , b and c initialised at 4.05438 Å. Visualised bond lengths of AlAs and AlSb were initiated at 2.75646 Å and 2.48279 Å respectively. AlAs_xSb_{1-x} configurations, with x values of 0.25 and 0.75, as well as 0.38 and 0.62 are considered 'reciprocal pairs', where the number of atoms and positions of As and Sb for all non-identical arrangements of composition were 'swapped' to produce the other (Refer to Figure 3.6).



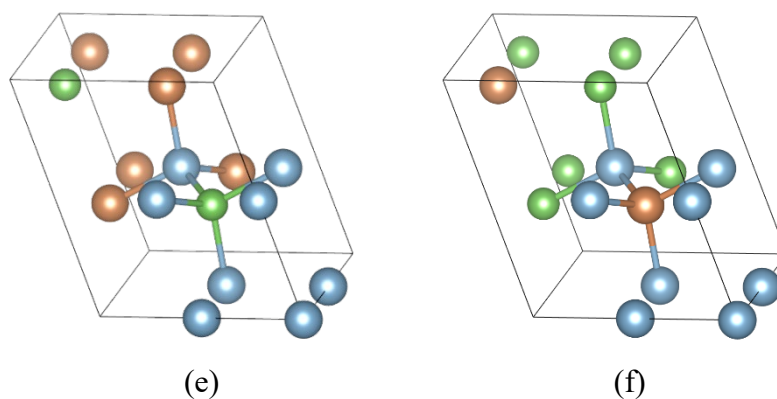
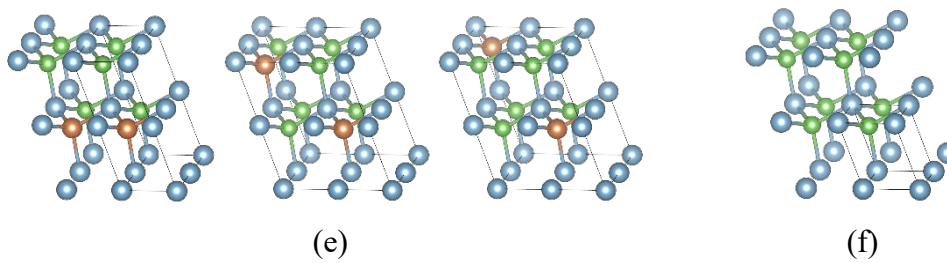
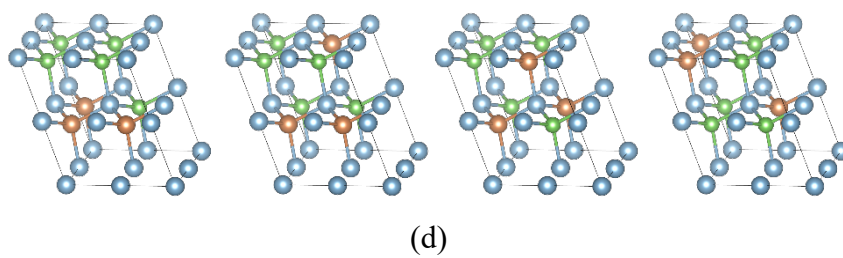
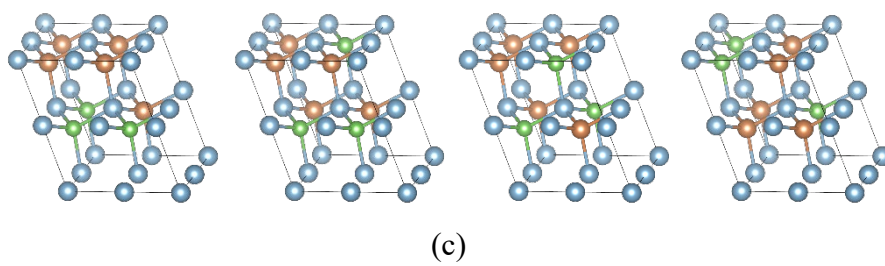
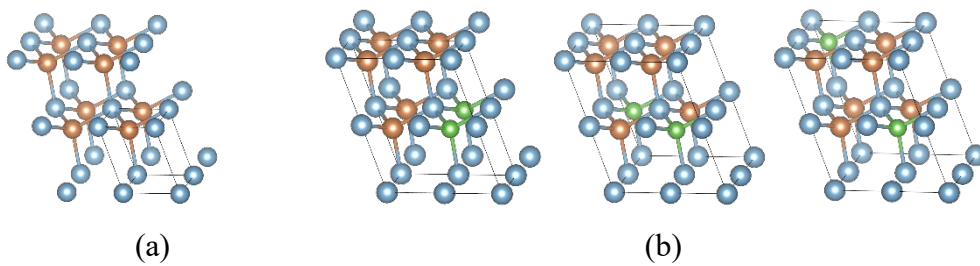


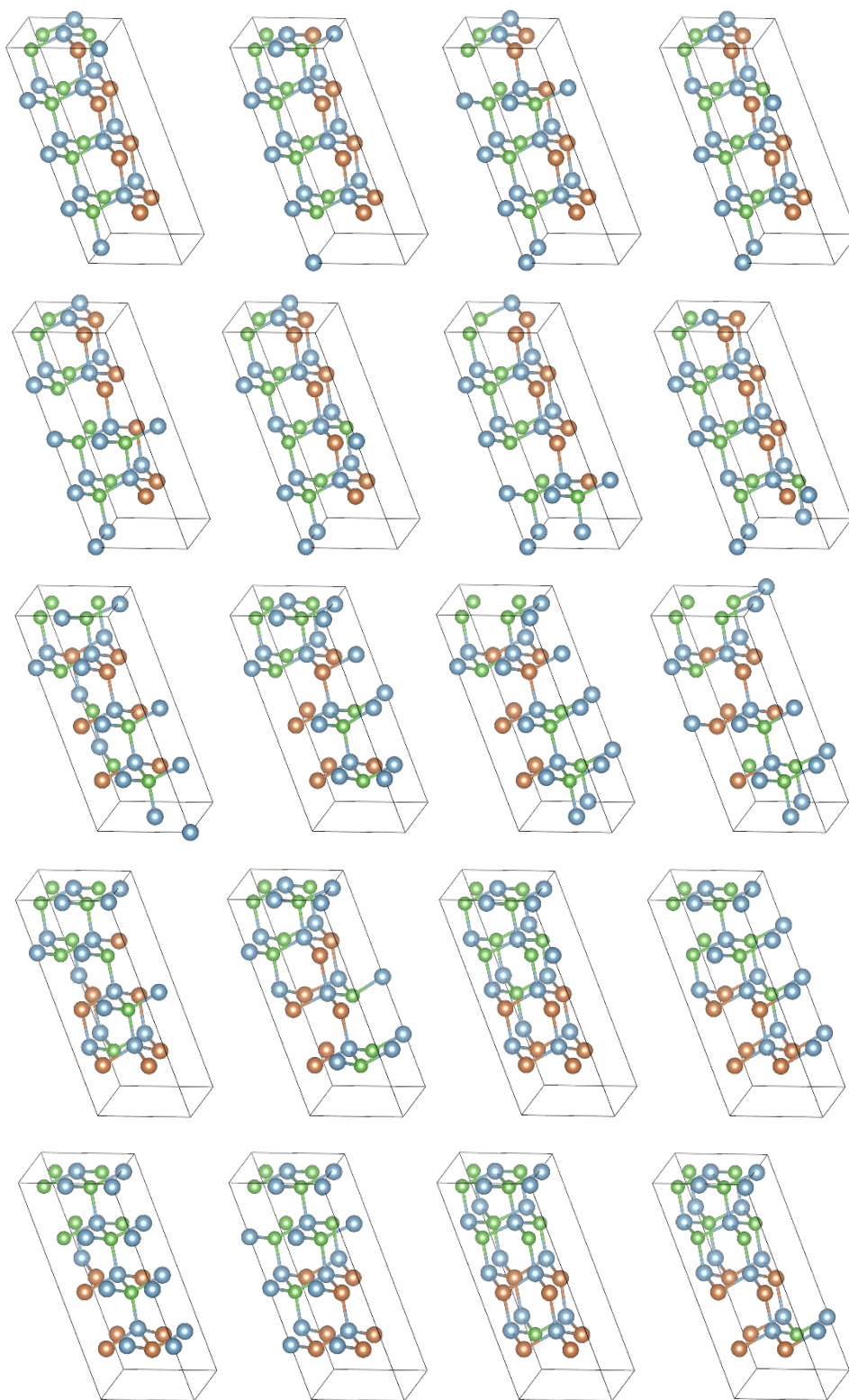
Figure 3.6: 3D projection of AlSb along the (a) x-axis, (b) y-axis and (c) z-axis and (d) angles $\alpha^{(e)}$, $\beta^{(e)}$ and $\gamma^{(e)}$, as indicated lattice parameters a , b and c . Visualization of ‘reciprocal pairs’ of constructed alloy composites (e) $\text{AlAs}_{0.25}\text{Sb}_{0.75}$ and (f) $\text{AlAs}_{0.75}\text{Sb}_{0.25}$. The blue, green and red spheres represent Al, As and Sb, respectively.

The following Figure 3.7 shows the visual representation of the set of non-identical $\text{AlAs}_x\text{Sb}_{1-x}$ unit cells that were assembled to be calculated and analysed. The orientation matrix shown in the diagrams are as follows:

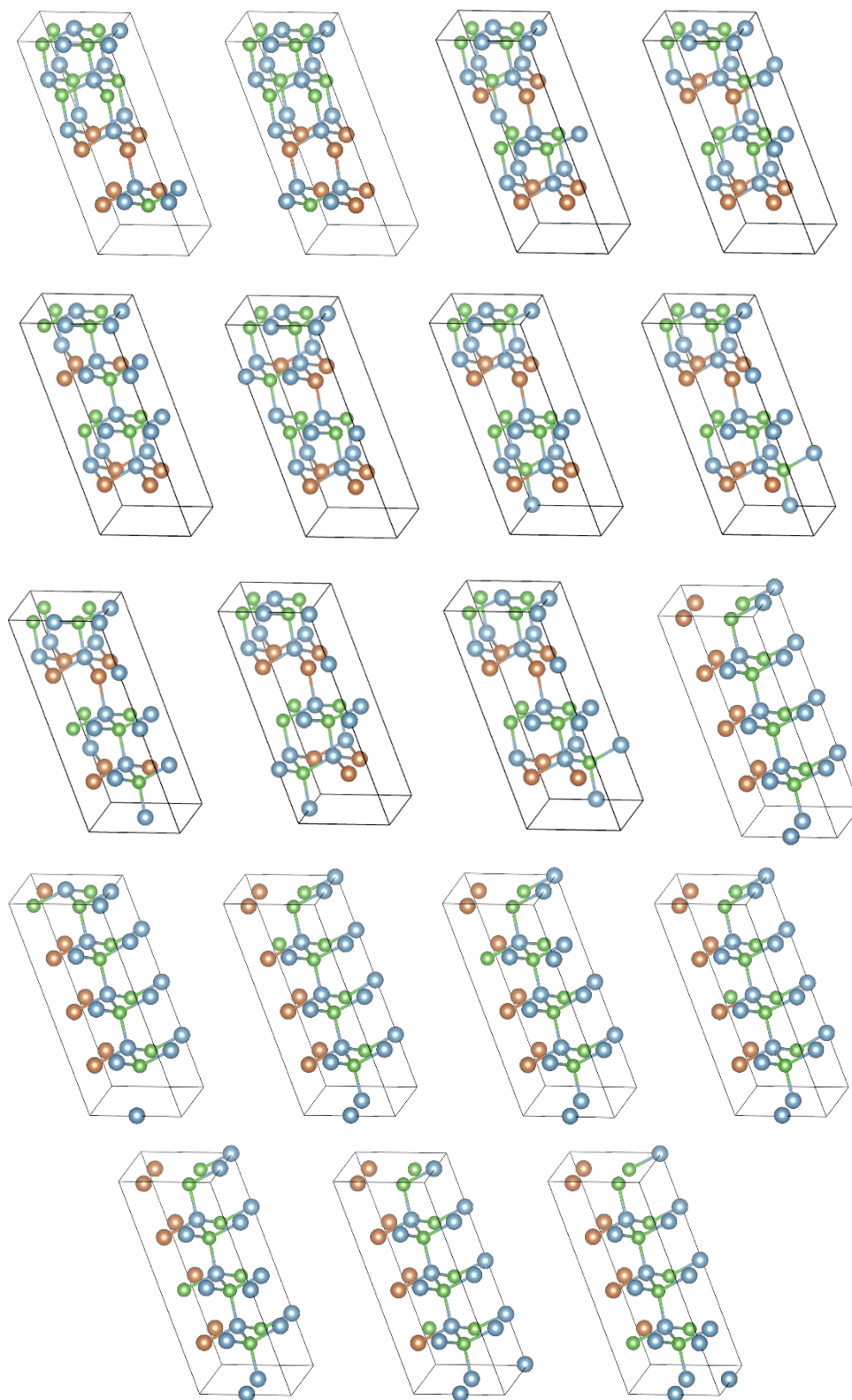
$$\begin{array}{ccc} -0.747639 & +0.049713 & +0.662242 \\ +0.010725 & +0.997968 & -0.062807 \\ -0.664019 & -0.039854 & -0.746653 \end{array}$$

XCrySDen, which is an acronym for Crystalline Structure and Densities is a visualization software and analyser program for the molecular and crystalline structure of studied materials, providing a three-dimensional visual representation of contours and molecular iso-surfaces while integrating user interactivity of graphic atomic structure (Kokalj, 1999). Distributed under the GNU General Public License, the latest 1.6.2 version released late 2019 typically runs on GNU/Linux systems, although it is also fully compatible with the MAC and Windows OS with additional requirements of supporting program extensions (Refer to Figure 3.8). First developed in 1996 and fully implementing three years later, the program is primarily used to visualize the crystal structure.





(g)



(g) continued

Figure 3.7: 3D visualization of the $\text{AlAs}_x\text{Sb}_{1-x}$ digital alloy composites where the value of x is (a) 0, (b) 0.25, (c) 0.38, (d) 0.62, (e) 0.75, (f) 1, and (g) 0.56. The blue, green and red spheres represent Al, As and Sb, respectively.

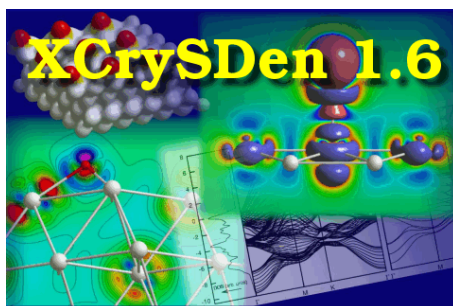


Figure 3.8: Logo of latest software built version of XCRYSDEN (Alexp, 2012).

XCRYSDEN software version 1.5.60 was utilized in gaining a convenient 3D visualization of the alloy composites, as shown in Figure 3.9. The visualized representation was toggled to display the supercell as a translational asymmetrical unit and configured to desired extended cell boundaries for further visual comparison and analysis of atomic positions, cell dimensions, lattice parameters and bond lengths. It was also employed to obtain the symmetrical k-points within the BZ after variable-cell relaxation is performed (Refer to Appendix A-1). This was done in order to map out the band structure k-points during preliminary study of the binary alloys.

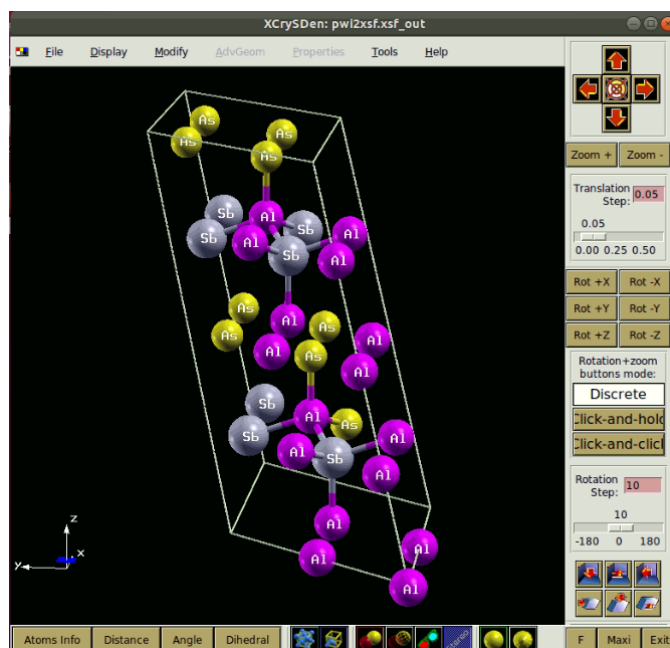


Figure 3.9: 3D visualization of one of the optimised $\text{AlAs}_x\text{Sb}_{1-x}$ alloy composites.

3.4 Performing Electronic-Structure Calculations

Calculations were performed and optimised through convergence tests, using pre-configured and parameters required for atomic relaxation and geometrical optimization. With defined properties and initialized values of the input files, the simulation was initiated and program functionalities were executed using Linux command codes within the terminal of the OS. Computations with included DFT exchange functional EV93 were specified for the alloy composites after performing relaxation.

Variable-cell relaxation, SCF and NSCF calculations require input parameters to be predetermined, which include, but are not limited to, atomic species, positions and cell parameters, convergence threshold values for both total and forces for ionic minimization, crystallographic constants, cut-off threshold values, type of convergence performed and the k-grid. Convergence threshold for ionic minimization on total energy and forces were set at 1×10^{-4} and 1×10^{-3} , respectively. Kinetic energy cut-off values for wavefunctions and also for charge density and potential convergence were configured at 40 Ry and 320 Ry, respectively. Gaussian smearing and Blöchl's tetrahedral method were implemented, with degauss value set at 0.01 Ry. With computations using the Marzari-Vanderbilt-DeVita-Payne cold smearing, the convergence threshold and mixing factors for self-consistency calculations were set at 1×10^{-7} and 0.5, respectively. Cell parameters and atomic positions were obtained via visualization performed using VESTA (Refer to Figure C-1, Appendix).

A flowchart of the main QE processes involved in these calculations are highlighted in Figure 3.10.

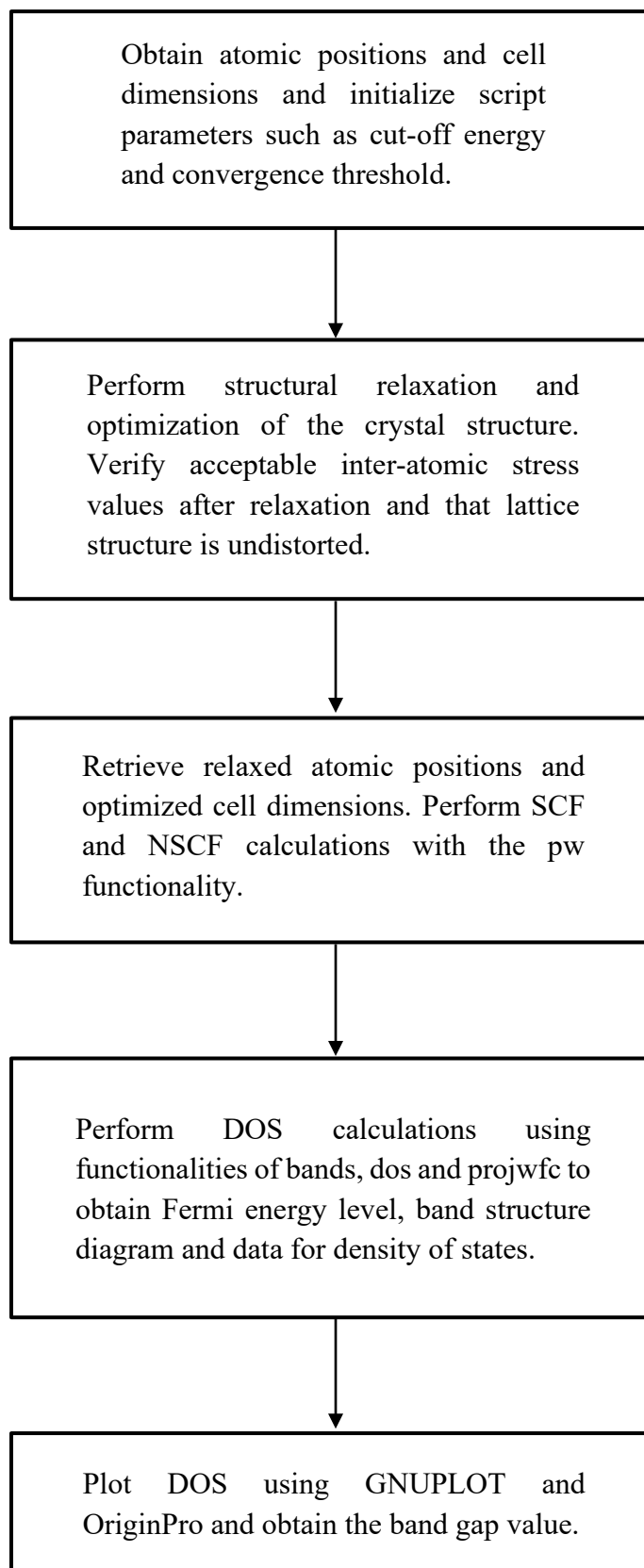


Figure 3.10: Flowchart for DFT calculations using Quantum ESPRESSO.

3.5 XC Functional and Parameters

The Perdew–Burke–Ernzerhof (PBE) exchange–correlation (XC) was implemented in this research project that performed scalar relativistic calculations using non-linear core corrections of Engel–Vosko (EV93) exchange functional. These calculations that were within the Generalized Gradient Approximation (GGA) functional framework, utilized the Troullier–Martins type Projector Augmented Wave (PAW) pseudopotential, which is based on the Kresse–Joubert research work (See Figure 3.11).

Geometrical optimization was performed via the Broyden–Fletcher–Goldfarb–Shanno (BFGS) algorithm, in which the Monkhorst-Pack k-mesh grid of $5 \times 5 \times 5$ was selected in the calculations of SCF, NSCF, and band structure of the AlAs and AlSb binaries and cell matrices $1 \times 2 \times 2$, $2 \times 2 \times 2$ and $2 \times 2 \times 4$ of the AlAs_xSb_{1-x} alloy composites. The noted high-symmetry points within the hexagonal lattice structure of the Brillouin zone are L, Γ , X, in which the path of the crystal k-points was $W \rightarrow L \rightarrow \Gamma \rightarrow X \rightarrow W \rightarrow K$. The motivation behind the selection of the k-point progression was mainly due to reference of the research paper in Nature Photonics (Yi *et al.*, 2019).

3.6 Work Plan

In this project, the research focus lies squarely on the electronic properties of AlAs_xSb_{1-x} by constructing the ternary alloy from either the AlAs or AlSb binary alloy composites. Preliminary study on binary alloys AlAs and AlSb will aid in the initialization and familiarization of the modelling and calculational processes required and consequently, providing a ground benchmark for computation parameters, calculated value range and accuracy of pseudopotentials employed. Subsequently, the focus is to measure the Fermi energy level, DOS, band gap energy and calculate the band structure of the supercells constructed, namely $1 \times 2 \times 2$, $2 \times 2 \times 2$ and $2 \times 2 \times 4$ matrices of the ternary alloys, and compare these values to determine if they are consistent with the literature and experimental values.

```

<UPF version="2.0.1">
<PP_INFO>
Generated using "atomic" code by A. Dal Corso v.5.0.2 svn rev.
9415
Author: ADC
Generation date: 11Sep2012
Pseudopotential type: PAW
Element: Al
Functional: SLA PW PBX PBC

Suggested minimum cutoff for wavefunctions: 36. Ry
Suggested minimum cutoff for charge density: 145. Ry
The Pseudo was generated with a Scalar-Relativistic Calculation
L component and cutoff radius for Local Potential: 2 1.9000

Valence configuration:
nl pn l occ Rcut Rcut US E pseu
3S 1 0 2.00 2.000 2.100 -0.569826
3P 2 1 1.00 2.000 2.100 -0.199338
Generation configuration:
3S 1 0 2.00 2.000 2.100 -0.569824
3S 1 0 0.00 1.400 2.100 6.000000
3P 2 1 1.00 2.000 2.100 -0.199338
3P 2 1 0.00 1.400 2.100 6.000000
3D 3 2 -2.00 1.900 1.900 -0.300000

<UPF version="2.0.1">
<PP_INFO>
Generated using "atomic" code by A. Dal Corso v.5.0.2 svn rev.
9415
Author: ADC
Generation date: 11Sep2012
Pseudopotential type: PAW
Element: As
Functional: SLA PW PBX PBC

Suggested minimum cutoff for wavefunctions: 20. Ry
Suggested minimum cutoff for charge density: 103. Ry
The Pseudo was generated with a Scalar-Relativistic Calculation
L component and cutoff radius for Local Potential: 2 2.0000

Valence configuration:
nl pn l occ Rcut Rcut US E pseu
4S 1 0 2.00 1.700 1.800 -1.065286
4P 2 1 3.00 1.900 2.000 -0.381818
Generation configuration:
4S 1 0 2.00 1.700 1.800 -1.065283
4S 1 0 0.00 1.700 1.800 0.400000
4P 2 1 3.00 1.900 2.000 -0.381816
4P 2 1 0.00 1.900 2.000 0.400000
4D 3 2 -2.00 2.000 2.000 0.500000

<UPF version="2.0.1">
<PP_INFO>
Generated using "atomic" code by A. Dal Corso v.6.2.2
Author: ADC
Generation date: 4May2018
Pseudopotential type: PAW
Element: Sb
Functional: SLA PW PBX PBC
Suggested minimum cutoff for wavefunctions: 27. Ry
Suggested minimum cutoff for charge density: 136. Ry
The Pseudo was generated with a Scalar-Relativistic
Calculation
Local Potential by smoothing AE potential with Bessel fncls,
cutoff radius: 2.1000
Pseudopotential contains additional information for GIPAW
reconstruction.
Valence configuration:
nl pn l occ Rcut Rcut US E pseu
5S 1 0 2.00 1.700 2.100 -0.943028
5P 2 1 3.00 1.700 2.500 -0.354838
Generation configuration:
5S 1 0 2.00 1.700 2.100 -0.943025
5S 1 0 0.00 1.700 2.100 6.300000
5P 2 1 3.00 1.700 2.500 -0.354837
5P 2 1 0.00 1.700 2.500 6.300000
5D 3 2 0.00 1.700 2.600 0.500000
5D 3 2 0.00 1.700 2.600 4.300000

```

Figure 3.11: Cropped PAW pseudo-potential script for (a) Al, (b) As and (c) Sb.

The alloy configurations are then visualized into interdigitated alloy composites, which involves replacing As atoms of the visualized AlAs supercell with a predetermined number of Sb atoms in an interdigitated arrangement, or alternatively, As atoms replacing Sb atoms in the AlSb supercell. The varied alloy configurations are to be arranged so that they are non-identical from one another, providing a number of possible configurations from which electronic properties are to be computed. Likewise, DOS, band gap, and band structure calculated for the composite alloys are matched against values that are reported in other research work, which are validated by implementing GGA (PAW) with the inclusion of DFT EV93.

Despite the enormous possibilities of alloy arrangement, specific arsenic compositions, x are selected in order to produce configurations that are closest to the fractions denoted applicable to as small a supercell repeat unit as

possible, due to limited computational resources and time constraint of this project. Ideally, at least three different interdigitated configurations of each fraction compositions are modelled to provide as equitable measurements as possible.

3.7 Work Stages

The work plan of this project consists of five main stages. The first stage involves the preliminary calculations of electronic properties of the binary alloys AlAs and AlSb. By initiating with known crystal structures, atomic positions and cell dimensions are obtained and structural relaxation is performed with appropriate PPs and computational parameters. The resulting optimized atomic positions and cell dimensions are then used to initiate the set of DFT calculations as requisite to procuring the DOS, band gap energy values and band structure of the alloys. The results are then analysed and the modelling processes are evaluated, in the event of redefining parameters for more accurate measurements.

The second stage extends the scope of the calculations through the crystal structure visualizations of interdigitated non-identical ternary alloy compositions $\text{AlAs}_x\text{Sb}_{1-x}$. Arsenic composition, x is selected to include at least five different configurations, from 0 to 1, inclusive. Empirical formula of the ternary alloy composites is determined to provide an overview of the possible cell matrices that can be constructed in the smallest possible repeat unit, as well as a set of fraction compositions that rounds up to the closest whole number of atoms that would allow for at least three different non-identical interdigitated configurations. Atomic positions and cell dimensions are mapped out and translated into QE input scripts for calculations (Refer to Figure C-1, Appendix).

The third stage consists of structural relaxation of the $\text{AlAs}_x\text{Sb}_{1-x}$ alloy composites to obtain ground state levels of optimized atomic positions and cell dimensions. An input file, each for the ternary alloy structures is created with initialization values and user-defined parameters, such as atomic species and coordinates, lattice vectors, crystallographic constants, and convergence threshold values (See Figure C-2, Appendix). Variable-cell relaxation is performed with the inclusion of EV93, from which the atomic coordinates and

crystal vectors are calibrated and calculated repeatedly until specified thresholds are met.

The fourth stage involves DFT self-consistent calculations from which NSCF and DOS computations are derived and performed. The Linux terminal command codes are then executed to initiate the SCF until the accuracy of computational energy levels and ground-state values reach the specified convergence threshold initialized. Procured data from SCF are requisites for consecutive NSCF and DOS computations that are to be carried out (See Figure C-3, C-4 and C-5, Appendix). The output files from these calculations produce structural and electronic properties, including but not limited to lattice parameters, Fermi energy level, total energy, kinetic energy cut-off values, threshold and field value accuracy, stress and pressure measurements. BANDS are calculated for supercells with symmetrical BZ, in which the band structures are mapped out for energy band gap value estimation (Refer to Figure C-6, Appendix).

The fifth stage entails the comparative analysis performed on the obtained DOS data and calculated energy band gap values. This also precludes any further adjustments and re-configurations of computational parameters and visualization of the crystal structure if large discrepancies and irregular values are procured and found in the process. The density of states and energy band gap values are thereby compared against experimental value and other results from literature.

CHAPTER 4

RESULTS AND DISCUSSION

4.1 Introduction

In this project, a preliminary study was conducted, where structural and electronic properties of zinc-blende alloys AlSb and AlAs were investigated. Energy band gap values, DOS and band structure were obtained from QE computations and analysed against other literary works and experimental data. Consequently, electronic properties of all visualized configurations of ternary alloy $\text{AlAs}_x\text{Sb}_{1-x}$ were methodically calculated and examined, acquiring data on DOS and band gap energies. The visualization, modelling and computation of the ternary alloy composites were performed on periodic, repeated nano-scale unit cells in a semiconductor material that could be extended into crystal structures of great dimensions, as pictures in Figure 4.1.

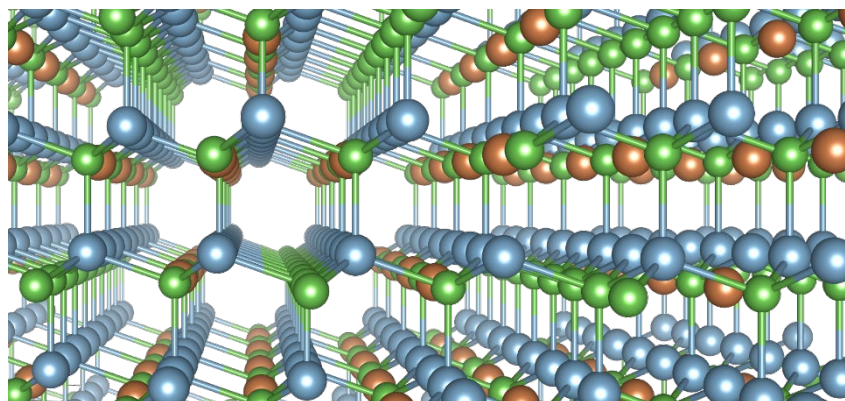


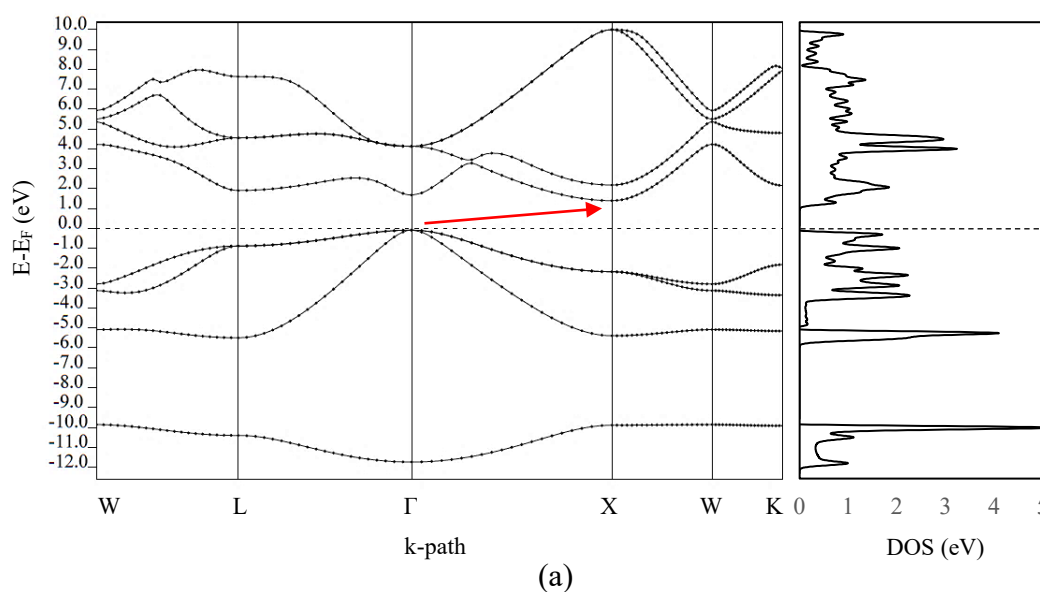
Figure 4.1: 3D illustration of finite crystal structure of one possible interdigitated configuration of $\text{AlAs}_x\text{Sb}_{1-x}$. The blue, green and red spheres represent Al, As and Sb, respectively.

Multiple computational attempts were made in order to adequately calibrate parameters to obtain data as accurate as possible, given the computational and time constraints. Results were tabulated and plotted with applied numerical and statistical analysis.

4.2 Electronic Properties of AIAs and AISb

The band structure in Figure 4.2 shows that both binary alloy composites have indirect bandgap, with gap measured at 1.22 eV between E_g^F (VBM) and E_g^L (CBM) for AISb and 1.48 eV between E_g^F (VBM) and E_g^X (CBM) for AIAs (Refer to Table 4.1).

As predicted, the DFT calculated energy gap values are underestimated, which is likely attributed by the self-interaction effects as well as the discontinuity derived from the exchange correlation (Bounab *et al.*, 2017). This is apparent when AIAs and AISb calculated values are compared against experimental values of 2.170 eV (Adachi, 2017) and 1.696 eV (Meyer, 2001) respectively. Nevertheless, the calculated values tallied closest to experimental values of XC functionals PBE and LDA of these alloy compounds, when the indirect band gaps are measured. Calculations are underestimated for AIAs and AISb on average by around 25 % and 15 %, respectively when comparatively analysed with WC-GGA, EV and EV93PW91. Despite the fact that GGA underestimates the energy gap values, it is generally accepted that the values obtained agree with that of experiment measurements of band structure and arrangement of energy levels. On top of that, the additional applied EV approach yields more accurate exchange potential and band splitting.



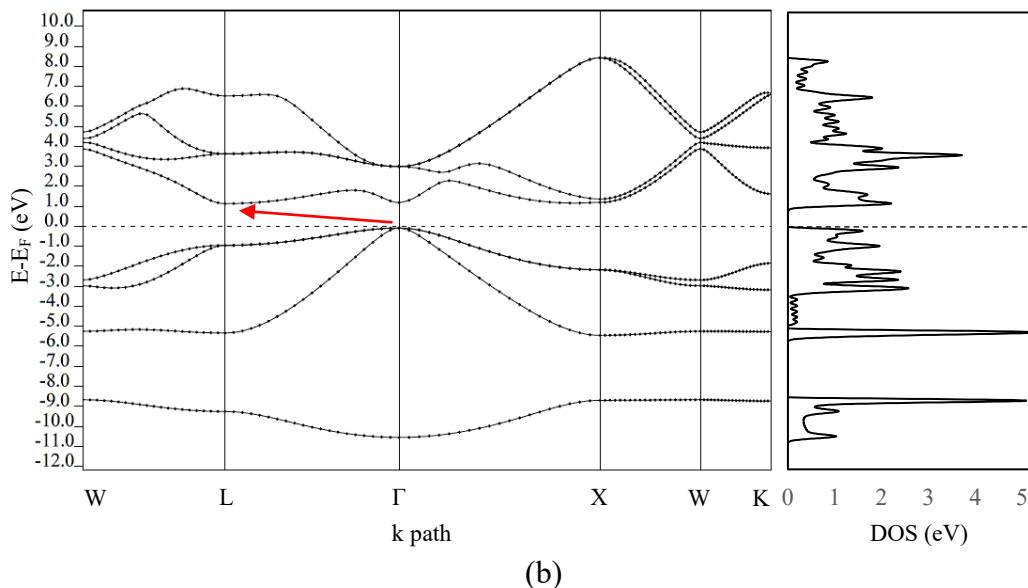


Figure 4.2: (a) Band structure diagram of (a) AlAs and (b) AlSb. The red bold arrow indicates the indirect band gap measured between VBM and CBM.

Table 4.1: Calculated band gap values of binary alloys AlAs and AlSb.

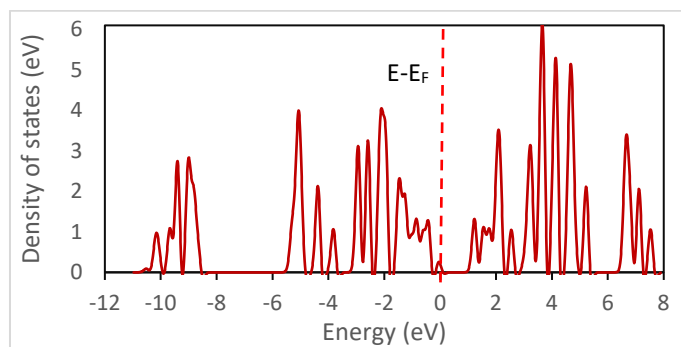
Alloy	k path	Calculated (eV)	Band gap type
AlAs	E_g^L	1.99	<i>indirect</i>
	E_g^X	1.48	<i>indirect</i>
	E_g^Γ	1.76	<i>direct</i>
AlSb	E_g^L	1.22	<i>indirect</i>
	E_g^X	1.25	<i>indirect</i>
	E_g^Γ	1.27	<i>direct</i>

4.3 Electronic Properties of $\text{AlAs}_x\text{Sb}_{1-x}$

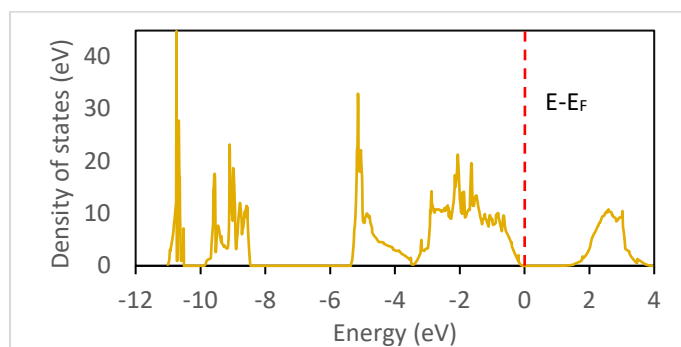
The density of state for $\text{AlAs}_x\text{Sb}_{1-x}$ alloy composites were computed by using the tetrahedral method. The average DOS were calculated from the aggregate of each of the alloy configurations and plotted in Figure 4.3, with indication of the $E-E_F$ level. It can be observed from DOS of the ternary alloys that the valence band consists of three distinct sections (Bounab *et al.*, 2017).

Assuming Y denotes both As and Sb for convenient representation, the first section is occupied by the s -states of the anion Y . The second section consists of s -states of cation Al and p -states of anion Y . The third section, located just below the Fermi level, E_F is occupied by the p -states of cation Al and anion Y . Both s - and p - states of the cation Al as well as p -states of Y dominate

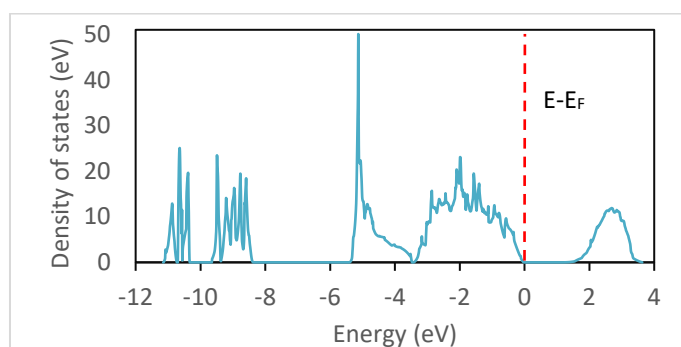
the conduction band, which also contribute to some perturbation of the minima within the conduction band.



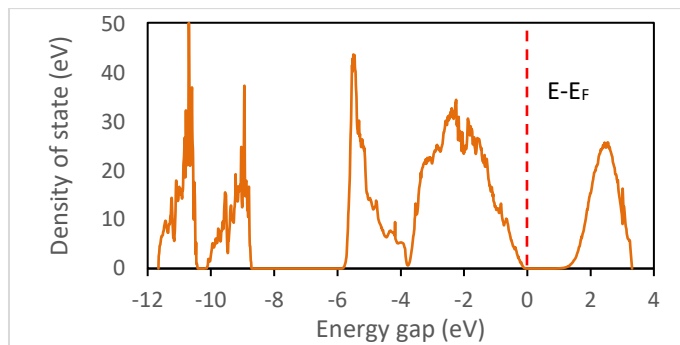
(a)



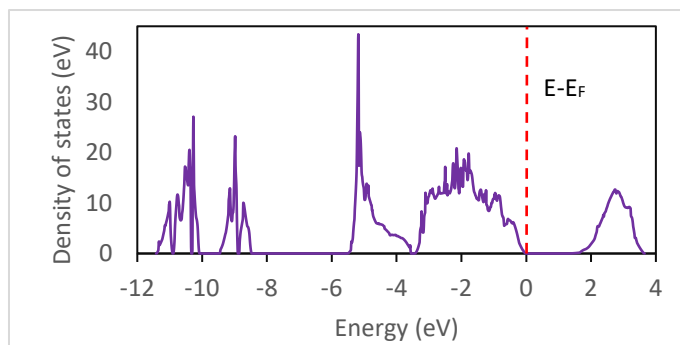
(b)



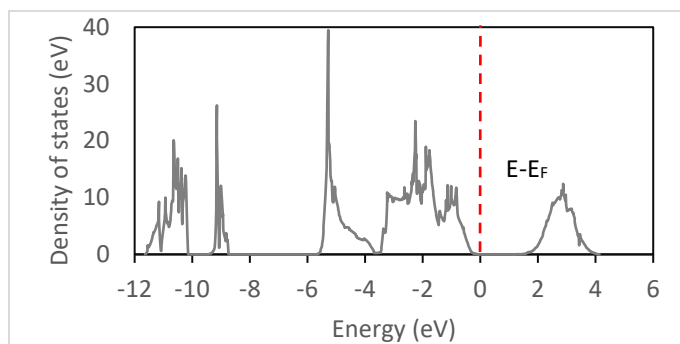
(c)



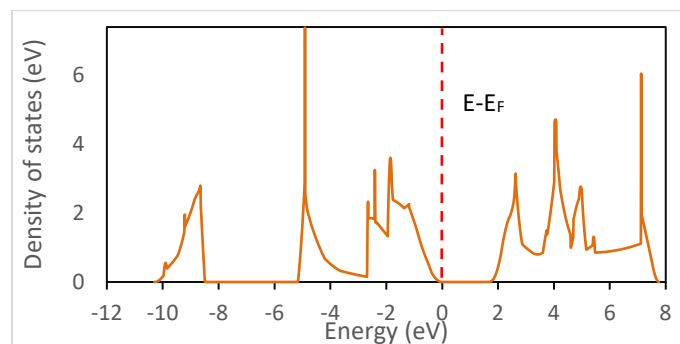
(d)



(e)



(f)

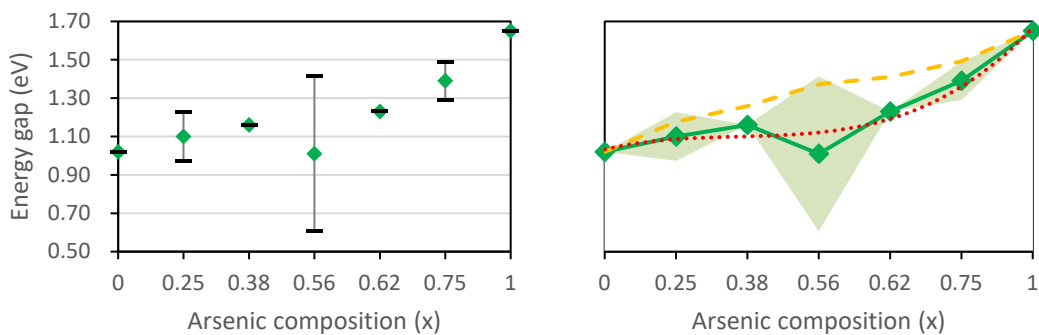


(g)

Figure 4.3: Calculated average density of state for $\text{AlAs}_x\text{Sb}_{1-x}$ alloy composite for values of x at (a) 0, (b) 0.25, (c) 0.38, (d) 0.56, (e) 0.62, (f) 0.75 and (g) 1. The red dash line indicates normalised Fermi energy level. $E-E_F$.

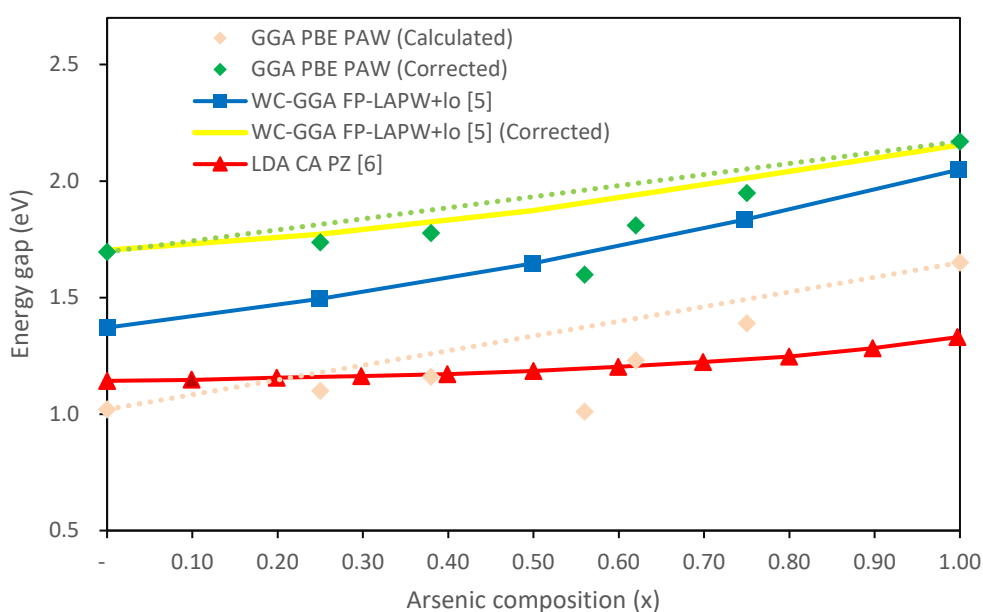
The energy band gap values are derived from the DOS and calculated Fermi energy level of the alloy configurations. The graph in Figure 4.4 plots the averaged band gap curves with standard deviation as well as graphical comparison with other experimental values. Standard deviation for 0.25 and 0.75 x values are 0.127 ± 0.003 eV and 0.10 ± 0.001 eV, respectively. The largest error can be distinctly seen in the configuration of 0.56 As composition with standard deviation of 0.404 ± 0.003 eV. 27 of the 39 configurations for $\text{AlAs}_{0.56}\text{Sb}_{0.44}$ alloy composite measured band gap values of less than 1 eV, while with the remaining 12, half of them had a band gap of 1.07 eV and the last six produced energy gap of more than 1.2 eV.

The underestimated of the energy band gap values were adjusted using the scissor-correction scheme (V. Fiorentini, 1995), which allows for the rigid shift in gap parameters in an attempt to more accurately fit the band gap curve with experimental range for binary alloys AlAs and AlSb. The scissor-corrected band gap curve was then compared against values by El Haj Hassan (2010) and Bounab (2017).



(a)

(b)



(c)

Figure 4.4: (a) Composition dependence of calculated energy band gap values with standard deviation bars and (b) shaded error bands with green dotted line representing Vegard's law. The orange dash line represents Vegard's law while the red dotted line is the bowed polynomial curve fitting. (c) Comparative analysis of scissor-corrected energy band gap values with experimental figures. The corresponding dotted lines represent Vegard's law applied to calculated band gap curves.

Energy band gap values calculated for all of the alloy compositions were fitted with a polynomial curve and analysed against Vegard's law,

represented by a corresponding dotted linear trendline. The linear regression slopes for the calculated band gap curve and scissor corrected curve are 0.63 and 0.464, respectively. These non-corrected calculated band gap curve is in agreement with the 0.62 - 0.65 range from experimental values of PBE and EV93PW91 (Tran and Blaha, 2017). The standard deviation of the band gap curve relative to Vegard's linear trendline was measured at 0.125 ± 0.005 eV.

The following expressions are derived from the polynomial curve fitting of the energy band gap values of the ternary alloy composites, where Equation 4.1 is the calculated PBE values, Equation 4.2 is WC-GGA (El Haj Hassan *et al.*, 2010) and Equation 4.3 is LDA (Bounab *et al.*, 2017)

$$y = 0.8457x^2 - 0.4115x + 1.7307 \quad (4.1)$$

$$y = 0.2119x^2 + 0.2456x + 1.7008 \quad (4.2)$$

$$y = 0.2039x^2 - 0.0297x + 1.1482 \quad (4.3)$$

There is some pronounced downward bowing or curvature of the $\text{AlAs}_x\text{Sb}_{1-x}$ alloys, indicating some deviation from Vegard's law. Comparative to the smaller bowing parameters of experimental values, the calculated data yielded greater bowing, which is largely due to the outlier band gap value of As composition, x at 0.56, as well as the lattice constants mismatch between binary alloy compounds AlAs and AlSb, at 4.05 Å and 4.41 Å, respectively. There is, however, clear indication of non-linear increase of the energy band gap values relative to the increase in the concentration of As.

Calculations obtained by Bounab (2017) were performed using DFT based ABINIT code, which is a prevalently employed basis-set, plane-wave DFT program, similar to that of Quantum Espresso operating through equivalent PPs. This is evident in the close proximate trend in the calculated band gap relative to Bounab's results. Although partially addressed by incorporating PAW, band gap underestimation is mainly due to the transferability of the PPS employed in the calculations concerning oscillations of the all-electron wavefunction (Hine, N., Dziedzic, J., Haynes, P., Skylaris, 2011). On the other hand, band gap measurements by El Haj Hassan (2010) were performed in WIEN2K code, which computes electronic band structure using more accurate linear augmented plane wave scheme in the method of local orbit. Consequently,

calculations using LDA or GGA approximations in WIEN2K includes relativistic and all-electronic calculations, which is apparent from the band gap curve shown with smaller adjustments using the scissor-correction scheme (Blaha. P., *et al.*, 2020).

CHAPTER 5

CONCLUSIONS AND RECOMMENDATIONS

5.1 Conclusions

In this report, the theoretical electronic properties of zinc-blende semiconductors of binaries AlAs and AlSb and ternary alloy $\text{AlAs}_x\text{Sb}_{1-x}$ were investigated through first principles DFT calculations using the PP of PBE PAW method of the electronic properties. Energy band gaps of AlAs and AlSb are in good agreement with values from literature and experimental figures, with indication of indirect band gaps namely via the CBM along the L- and X-paths of the band structures. The calculated band gap values, E_g of AlAs and AlSb are 1.48 eV and 1.22 eV respectively, which is well within the range reported by other authors of 1.32 eV to 1.78 eV for AlAs and 0.99 eV to 1.40 eV for AlSb.

Electronic properties of ternary alloy composite $\text{AlAs}_x\text{Sb}_{1-x}$ have also yielded similar non-linear relationship between the two constituent binary alloys, which is in concurrence with values reported by El Haj Hassan *et al.* and Bounab *et al.* after applying the scissor-correction scheme, which is an indication of the deviation from Vegard's law. There is also clear energy gap dependence on the arsenic composition, x with noticeable downward bowing of the ternary alloys of 0.85.

The band gap values based on Arsenic dependence produced by El Haj Hassan using the WIEN2k code was shown to be less underestimated than the QE calculated values and values measured by Bounab using the Abinit code. The studies on the $\text{AlAs}_x\text{Sb}_{1-x}$ alloy composites and results obtained from this project can serve as predictions and guided indications, which may warrant future investigative work for more accurate band gap estimation.

5.2 Recommendations for Future Work

As there are discrepancies of the energy gap values between composites with x value of 0.56, seen as an outlier compared to the rest of the data, remedial

efforts may be attempted, which will also affect the bowing parameter, b of the band gap curve to a value that is more in agreement with literature. Firstly, it may prudent that visualizations of additional crystal structures of supercell matrices matching that of x value 0.56 be added to the array, with ensuing structural relaxations and SCF calculations be performed in order to more accurately obtain average values of the energy band gap across the entire range of arsenic composition.

It was shown that using DOS to derive the ternary alloy energy gap produced values that are grossly underestimated, in comparison to band gap values calculated for the binary alloys that were directly derived from calculated band structures. The reasoning behind using DOS was that the BZ of the supercell structures were highly distorted, with no clear approximate k-points indicating the crucial X-, L- and Γ -paths (Refer to Figure A-1, Appendix). Therefore, it is recommended that during the initial visualization work phase, the supercells constructed should have similar symmetrical BZ structures to that of the constituent binaries AlAs and AlSb, with crystal k-points of $W \rightarrow L \rightarrow \Gamma \rightarrow X \rightarrow W \rightarrow K$. This would allow the band structures to be accurately mapped and the energy gap values more accurately measured.

As accurate estimation of the fundamental energy gap is important and is mainly attributed to the measurement of the three main conduction band minimum points, in the case of indirect band gap material like AlAs and AlSb, there have been attempts in determining the crossover point where the CBM of intermediate ternary alloys shifts from L to X k-paths (El Haj Hassan *et al.*, 2010). It may be recommended that alloy composition, x be specifically visualized and modelled so that calculations can provide some narrow band indications where the crossover from indirect to direct band gap occurs, identifying a critical x value where energy values along the Γ -path is approximately the same energy as along the X k-path.

Random alloy calculations that were initially planned and attempted took considerably long periods of time to be completed and was proven to be unsuccessful, the latter of which may be due to the crystal structure geometry and other unexpected factors. As the triclinic structure was initially

implemented, one recommendation is for visualization of the random alloys to be in other crystal structures, such as simple cubic and tetragonal cell.

In terms of accurately describing a macroscopically isotropic random alloys in a periodic structure, an extremely and sufficiently large supercell is required for DFT structural relaxation and SCF calculations and this too provides computational challenge in terms of resources available. As Zunger et al. had implemented the approach of using Special Quasi-random Structures (SQS) which produces a close approximation of isotopically random structures confined to the first several shells within the locality of the modelled structure (El Haj Hassan *et al.*, 2010). This, thus suspends any periodicity errors further away from the central region and towards neighbouring regions of the supercells and would allow for computations that are reasonably executable while still effectively calculating structural and electronic properties that resemble random alloy supercells. In addition to alternative visualization of the random alloy composites, the supercells may incorporate SQS in the suggested cell matrices of $3 \times 3 \times 3$.

REFERENCES

- A. Jain, S.P. Ong, G. Hautier, W. Chen, W.D. Richards, S. Dacek, S. Cholia, D. Gunter, D. Skinner, G. Ceder, K. A. P. (2013) ‘The Materials Project: A materials genome approach to accelerating materials innovation’, *APL Materials*, 1(1). Available at: <https://materialsproject.org/>.
- Adachi, S. (2017) ‘III-V Ternary and Quaternary Compounds’, in *Springer Handbooks*, pp. 725–741. doi: 10.1007/978-3-319-48933-9_30.
- Alexp (2012) *Index of /afs/athena/software/xcrysdn_v1.5.60/distrib/i386_ubuntu1404/xcrysdn-1.5.60/images, Athena.mit.edu. Available at: https://stuff.mit.edu/afs/athena/software/xcrysdn_v1.5.60/distrib/i386_ubuntu1404/xcrysdn-1.5.60/images/*.
- Ashcroft, A. R. D. and N. W. (1991) ‘Vegard’s law’, *PHYSICAL REVIEW A*, 43(3161). doi: <https://doi.org/10.1103/PhysRevA.43.3161>.
- Blaaha, P., Schwarz, K., Tran, F., Laskowski, R., Madsen, G., and Marks, L. (2020) ‘WIEN2k: An APW+lo program for calculating the properties of solids’, *The Journal of Chemical Physics*, 152(074101). doi: <https://doi.org/10.1063/1.5143061>.
- Bounab, S. *et al.* (2017) ‘First-Principles Calculations of Structural, Electronic and Optical Properties of Ternary Semiconductor Alloys ZAs_xSb_{1-x} (Z = B, Al, Ga, In)’, *Journal of Electronic Materials*, 46(8), pp. 4805–4814. doi: 10.1007/s11664-017-5425-9.
- Dalcorso (2012) *Welcome to pslibrary A library of ultrasoft and PAW pseudopotentials, GitHub Pages. Available at: https://dalcorso.github.io/pslibrary/*.
- V. Fiorentini, A. B. (1995) ‘Dielectric scaling of the self-energy scissor operator in semiconductors and insulators’, *Physical Review B - Condensed Matter and Materials Physics*, 51(23). doi: <https://doi.org/10.1103/PhysRevB.51.17196>.
- Giannozzi, P., Baroni, S., Bonini, N., Calandra, M., Car, R., Cavazzoni, C., Ceresoli, D., Chiarotti, G.L., Cococcioni, M., Dabo, I. and Dal Corso, A. (2002) ‘QUANTUM ESPRESSO: a modular and open-source software project for quantum simulations of materials’, *Journal of physics: Condensed matter*, 21(39), p. 395502.
- Giannozzi, P. *et al.* (2017) ‘Advanced capabilities for materials modelling with Quantum ESPRESSO’, *Journal of Physics Condensed Matter*, 29(46). doi: 10.1088/1361-648X/aa8f79.

El Haj Hassan, F. *et al.* (2010) 'First-principles study of the ternary semiconductor alloys (Ga,Al)(As,Sb)', *Journal of Alloys and Compounds*, 499(1), pp. 80–89. doi: 10.1016/j.jallcom.2010.02.121.

Heyd, J. *et al.* (2005) 'Energy band gaps and lattice parameters evaluated with the Heyd-Scuseria-Ernzerhof screened hybrid functional', *Journal of Chemical Physics*, 123(17). doi: 10.1063/1.2085170.

Hine, N., Dziedzic, J., Haynes, P., Skylaris, K. (2011) 'Electrostatic interactions in finite systems treated with periodic boundary conditions: Application to linear-scaling density functional theory', *The Journal of Chemical Physics*, 135(204103). doi: <https://doi.org/10.1063/1.3662863>.

Hinuma, Y. *et al.* (2014) 'Band alignment of semiconductors from density-functional theory and many-body perturbation theory', *Physical Review B - Condensed Matter and Materials Physics*, 90(15), pp. 1–16. doi: 10.1103/PhysRevB.90.155405.

Jain, A. *et al.* (2013) 'Commentary: The materials project: A materials genome approach to accelerating materials innovation', *APL Materials*, 1(1). doi: 10.1063/1.4812323.

King, H. W. (1966) 'Quantitative size-factors for metallic solid solutions', *Journal of Materials Science*, 1, pp. 79–90. Available at: <https://link.springer.com/article/10.1007/BF00549722>.

Koichi Momma, F. I. (2011) 'VESTA 3 for three-dimensional visualization of crystal, volumetric and morphology data', *Journal of Applied Crystallography*, 44(6), pp. 1272–1276. doi: <https://doi.org/10.1107/S0021889811038970>.

Kokalj, A. (1999) 'XCrySDen-a new program for displaying crystalline structures and electron densities', *Journal of Molecular Graphics and Modelling*, 17(3–4), pp. 176–179. doi: 10.1016/S1093-3263(99)00028-5.

Meyer, I. V. and J. R. (2001) 'Band parameters for III–V compound semiconductors and their alloys', *Journal of Applied Physics*, 89(5815). doi: <https://doi.org/10.1063/1.1368156>.

Momma, K. (2021) *Software VESTA, JP-Minerals*. Available at: <https://jp-minerals.org/vesta/en/>.

QEF (2019) *Quantum ESPRESSO Pseudopotentials, Quantum ESPRESSO Foundation*. Available at: http://pseudopotentials.quantum-espresso.org/legacy_tables/ps-library.

QEF (2021) *Quantum ESPRESSO, Quantum ESPRESSO Foundation*.

Available at: <https://www.quantum-espresso.org/>.

Rubio, A. and Marques, M. (2009) ‘Time-dependent density-functional theory’, *Physical Chemistry Chemical Physics*, 11(22), p. 4436. doi: 10.1039/b908105b.

Tran, F. and Blaha, P. (2017) ‘Importance of the Kinetic Energy Density for Band Gap Calculations in Solids with Density Functional Theory’, *Journal of Physical Chemistry A*, 121(17), pp. 3318–3325. doi: 10.1021/acs.jpca.7b02882.

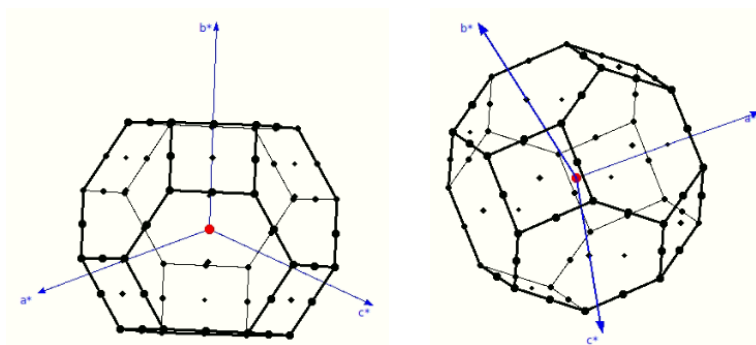
Wadehra, A., Nicklas, J. W. and Wilkins, J. W. (2010) ‘Supplementary information’, *Applied Physics Letters*, 97, p. 092119.

Yi, X. *et al.* (2019) ‘Extremely low excess noise and high sensitivity AlAs_{0.56}Sb_{0.44} avalanche photodiodes’, *Nature Photonics*, 13(10), pp. 683–686. doi: 10.1038/s41566-019-0477-4.

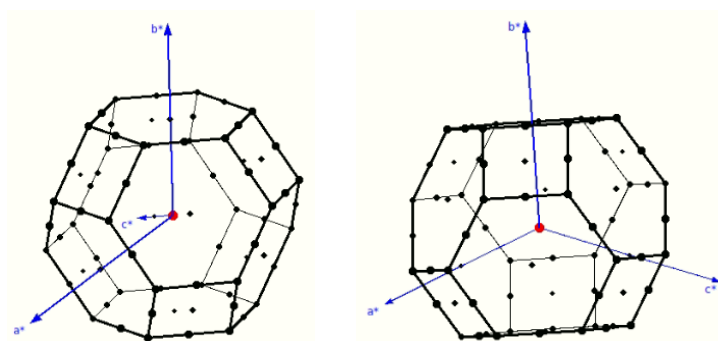
Zunger, J. E. B. and A. (1986) ‘Optical bowing in zinc chalcogenide semiconductor alloys’, *Physical Review B - Condensed Matter and Materials Physics*, 34(5992). doi: <https://doi.org/10.1103/PhysRevB.34.5992>.

APPENDICES

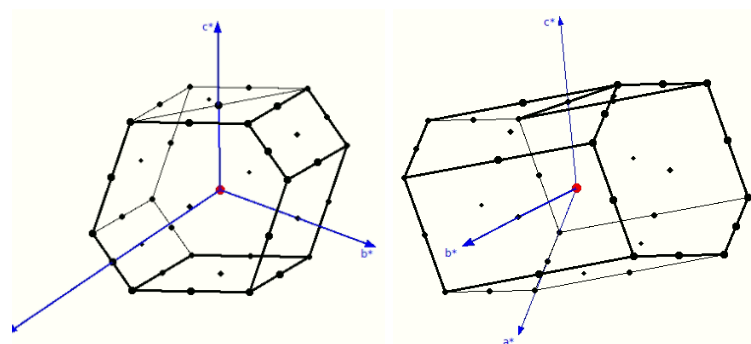
APPENDIX A: Figures and Graphs



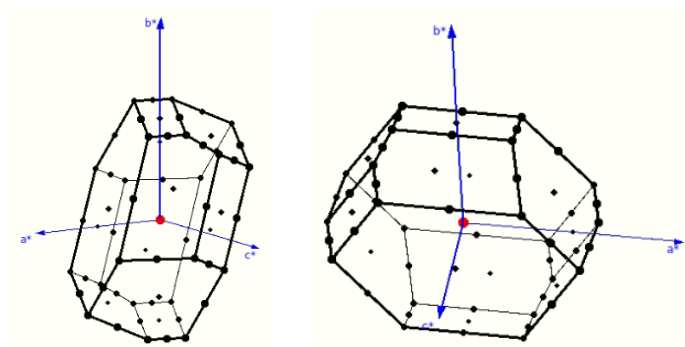
(a)



(b)



(c)



(d)

Figure A-1: Brillouin zones for supercells of x values and cell matrices (a) 0 and 1 ($1 \times 1 \times 1$), (b) 0.25, 0.38, 0.62 and 0.75 ($2 \times 2 \times 2$), (c) 0.25 and 0.75 ($1 \times 2 \times 2$) and (d) 0.56 ($2 \times 2 \times 4$).

APPENDIX B: Tables

Table B-1: Structural, electronic and optical properties of binary alloys AlAs and AlSb (Adachi, 2017).

Description	Binary Alloy	
	AlAs	AlSb
Lattice parameter, a (Å)	5.66139	6.1355
Crystal density, ρ (g/cm ³)	3.7302	4.2775
Elastic stiffness, C_{ij} (10 ¹¹ dyn/cm ²)		
C11	11.930	8.769
C12	5.720	4.341
C44	5.720	4.076
Compliance constants, S_{ij} (10 ⁻¹² cm ² /dyn)		
S11	1.216	1.697
S12	-0.3940	-0.5618
S44	1.748	2.453
Specific heat, C (J/(gK))	0.424	0.326
Debye temperature, θ_D (K)	450	370
Linear thermal expansion coefficient, α_{th} (10 ⁻⁶ K ⁻¹)	4.1	4.2
Thermal resistivity, W (cm K/W)	1.10	1.75
Bandgap energies		
E_0 (eV)	3.01	2.27
E_g^X (eV)	2.15	1.615
E_g^L (eV)	2.37	2.211
E_1 (eV)	3.62 - 3.90	2.78 - 2.890
E_2 (eV)	4.853, 4.89	4.20 - 4.25
Electron effective mass at gamma		
m_e^Γ/m_0	0.124	0.14
Density of state mass		
m_e^X/m_0	0.71	0.84
m_e^L/m_0	0.78	1.05
Conductivity mass		
m_c^X/m_0	0.26	0.29
m_c^L/m_0	0.21	0.28
Density of states heavy hole		
m_{HH}^*/m_0	0.81	0.9
Averaged light hole		
m_{LH}^*/m_0	0.16	0.13
Spin orbit split-off effective hole masses		
m_{SO}	0.30	0.317
Conduction band deformation potentials		
a_c (eV)	-5.64	-6.97

Valence band deformation potentials		
a_v (eV)	-2.60	1.38
b (eV)	-2.3	-1.35
d (eV)	-	-4.3
<hr/>		
Dielectric constant		
ϵ_s	10.06	11.21
ϵ_∞	8.16	9.88
<hr/>		
Hall mobilities		
Electrons, μ_e (cm ² /V s)	294	200
Holes, μ_h (cm ² /V s)	105	420
<hr/>		

APPENDIX C: Computer Command Scripts

<pre> All As1 1.0 4.054377558 0.000000000 0.000000000 4.0543770883 7.0223881897 0.000000000 4.0543770883 2.3407958833 6.6207711424 Al As Sb 4 1 3 Cartesian 0.00000000 0.00000000 0.00000000 2.027188423 1.170397872 3.310385374 2.027188544 3.511194095 0.000000000 4.054376967 4.681591967 3.310385374 6.081565862 3.511194097 2.482789376 8.108754044 4.681591969 5.793174750 8.108754406 7.022388192 2.482789376 10.135943313 8.192786064 5.793174750 </pre>	<pre> 22 All As1 Al 0.000000 0.000000 0.000000 Al 4.054377 2.340796 6.620771 Al 4.054377 7.022388 0.000000 Al 8.108754 9.363184 6.620771 Al 4.054378 0.000000 0.000000 Al 8.108755 2.340796 6.620771 Al 8.108755 7.022388 0.000000 Al 12.163132 9.363184 6.620771 Al 2.027188 1.170398 3.310385 Al 6.081566 8.192786 3.310385 Al 6.081566 1.170398 3.310385 Al 10.135943 8.192786 3.310385 Al 2.027189 3.511194 0.000000 Al 6.081566 5.851990 6.620771 Al 6.081566 3.511194 0.000000 Al 10.135943 5.851990 6.620771 Al 4.054377 4.681592 3.310385 Al 8.108755 4.681592 3.310385 As 6.081566 3.511194 2.482789 Sb 8.108754 4.681592 5.793175 Sb 8.108754 7.022388 2.482789 Sb 10.135943 8.192786 5.793175 </pre>
(a)	(b)

Figure C-1: Sample VESTA output scripts of atomic positions and dimensions in the format of (a) *.vasp* and (b) *.xyz*.

```

|&CONTROL
    calculation = 'vc-relax',
    outdir = './outdir',
    pseudo_dir = './',
    prefix = 'AlAsSb',
    tstress = .true.,
    tprnfor = .true.,
    etot_conv_thr = 1.00-4,
    forc_conv_thr = 1.00-3,
    nstep = 500,
/
&SYSTEM
    ibrav = 0,
    !celldm(1) = 7.66166623984036,
    nat = 8,
    ntyp = 3,
    ecutwfc = 40,
    ecutrho = 320,
    occupations = 'smearing',
    degauss = 0.01,
    smearing = 'mv'
/
&ELECTRONS
    conv_thr = 1.0d-7,
    mixing_beta = 0.5
/
&ions
    ion_dynamics = 'bfgs'
/
&cell
    cell_dynamics = 'bfgs'
/
ATOMIC_SPECIES
Al 26.981539 Al.pbe-n-kjpaw_psl.0.1.UPF
Sb 121.76 Sb.pbe-n-kjpaw_psl.1.0.0.UPF
As 74.9216 As.pbe-n-kjpaw_psl.0.2.UPF
CELL_PARAMETERS (angstrom)
  4.054377558      0.000000000      0.000000000
  4.0543770883    7.0223881897      0.000000000
  4.0543770883    2.3407958833      6.6207711424
ATOMIC_POSITIONS (angstrom)
Al 0.000000000      0.000000000      0.000000000
Al 2.027188423    1.170397872      3.310385374
Al 2.027188544    3.511194095      0.000000000
Al 4.054376967    4.681591967      3.310385374
As 6.081565862    3.511194097      2.482789376
Sb 8.108754044    4.681591969      5.793174750
Sb 8.108754406    7.022388192      2.482789376
Sb 10.135943313   8.192786064      5.793174750
K_POINTS automatic
5 5 5 0 0 0

```

Figure C-2: Sample QE input script for structural relaxation VCRELAX parameters.

```

| &CONTROL
      calculation = 'scf' ,
      outdir = './outdir',
      pseudo_dir = './',
      prefix = 'AlAsSb',
      tstress = .true.,
      tprnfor = .true.,
      etot_conv_thr = 1.0D-4,
      forc_conv_thr = 1.0D-3,
      nstep = 500,
/
&SYSTEM
      ibrav = 0,
      !celldm(1) = 7.66166623984036
      nat = 8,
      ntyp = 3,
      ecutwfc = 40,
      ecutrho = 320,
      occupations = 'smearing',
      degauss = 0.01,
      smearing = 'mv',
      input_dft = 'ev93'
/
&ELECTRONS
      conv_thr = 1.0d-7,
      mixing_beta = 0.5
/

ATOMIC_SPECIES
Al 26.981539 Al.pbe-n-kjpaw_psl.0.1.UPF
Sb 121.76 Sb.pbe-n-kjpaw_psl.1.0.0.UPF
As 74.9216 As.pbe-n-kjpaw_psl.0.2.UPF

CELL_PARAMETERS (angstrom)
4.324934570 0.000000017 0.000000012
4.324934101 7.471629128 -0.004639457
4.324934101 2.486168729 7.045865714

ATOMIC_POSITIONS (angstrom)
Al 0.000000000 0.0044403383 0.0031397604
Al 2.1624669218 1.3440088741 3.4789498443
Al 2.1624670508 3.7279881605 0.1074934908
Al 4.3249339715 4.8821414255 3.4521953730
As 6.4874013748 3.7355354225 2.6414223458
Sb 8.6498680392 4.9842052896 6.1582472165
Sb 8.6498684254 7.4674534238 2.6464051449
Sb 10.8123358631 8.7065196165 6.1564387620

K_POINTS automatic
5 5 5 0 0 0

```

Figure C-3: Sample QE input script of SCF parameters.

```

&CONTROL
    calculation = 'nscf' ,
    outdir = './outdir',
    pseudo_dir = './',
    prefix = 'AlAsSb',
    tstress = .true.,
    tprnfor = .true.,
    etot_conv_thr = 1.0D-4,
    forc_conv_thr = 1.0D-3,
    nstep = 500,
/
&SYSTEM
    ibrav = 0,
    !celldm(1) = 7.66166623984036
    nat = 8,
    ntyp = 3,
    ecutwfc = 40,
    ecutrho = 320,
    occupations = 'tetrahedra',
    degauss = 0.01,
    smearing = 'mv',
    input_dft = 'ev93'
/
&ELECTRONS
    conv_thr = 1.0d-7,
    mixing_beta = 0.5
/

ATOMIC_SPECIES
Al 26.981539 Al.pbe-n-kjpaw_psl.0.1.UPF
Sb 121.76 Sb.pbe-n-kjpaw_psl.1.0.0.UPF
As 74.9216 As.pbe-n-kjpaw_psl.0.2.UPF

CELL_PARAMETERS (angstrom)
4.324934570 0.000000017 0.000000012
4.324934101 7.471629128 -0.004639457
4.324934101 2.486168729 7.045865714

ATOMIC_POSITIONS (angstrom)
Al 0.000000000 0.0044403383 0.0031397604
Al 2.1624669218 1.3440088741 3.4789498443
Al 2.1624670508 3.7279881605 0.1074934908
Al 4.3249339715 4.8821414255 3.4521953730
As 6.4874013748 3.7355354225 2.6414223458
Sb 8.6498680392 4.9842052896 6.1582472165
Sb 8.6498684254 7.4674534238 2.6464051449
Sb 10.8123358631 8.7065196165 6.1564387620

K_POINTS automatic
5 5 5 0 0 0

```

Figure C-4: Sample QE input script of NSCF parameters.

```

&DOS
  outdir = './outdir' ,
  prefix = 'AlAsSb' ,
  fildos = 'AlAsSb_1x2x2_C1.dos',
  !Emin = -12,
  !Emax = 12,
/

```

Figure C-5: Sample QE input script of DOS parameters.

```

|&CONTROL
  calculation = 'bands',
  outdir = './outdir',
  pseudo_dir = './',
  prefix = 'AlAs',
  tstress = .true.,
  tprnfor = .true.,
  etot_conv_thr = 1.00-4,
  forc_conv_thr = 1.00-3,
  nstep = 500,
/
&SYSTEM
  ibrav = 0,
  !celldm(1) = 7.66166623984036,
  nat = 2,
  ntyp = 2,
  ecutwfc = 40,
  ecutrho = 320,
  occupations = 'smearing',
  degauss = 0.01,
  smearing = 'mv'
/
&ELECTRONS
  conv_thr = 1.0d-7,
  mixing_beta = 0.5
/
&ions
  ion_dynamics = 'bfgs'
/
&cell
  cell_dynamics = 'bfgs'
/
ATOMIC_SPECIES
Al 26.981539 Al.pbe-n-kjpaw_psl.0.1.UPF
As 74.9216 As.pbe-n-kjpaw_psl.0.2.UPF
CELL_PARAMETERS (angstrom)
4.053918130 0.000000000 0.000000000
2.026959065 3.510796085 -0.000000000
2.026959065 1.170265362 3.310014775
ATOMIC_POSITIONS (angstrom)
Al -0.000000000 0.000000000 -0.0000009358
As 6.0808771947 3.5107960852 2.4825120169
K_POINTS {crystal_b}
6
0.50000 -0.25000 0.25 20
0.00000 -0.50000 0.00 20
0.00000 0.00000 0.00 20
0.50000 0.00000 0.50 20
0.50000 -0.25000 0.25 20
0.37500 -0.37500 0.00 20

```

Figure C-6: Sample QE input script of BANDS parameters for binary alloy.